Aalto University
School of Engineering

School of Engineering
Degree Programme of Structural Engineering and Building Technology

Simon Burck

A METHOD FOR REVIEWING STRUCTURAL SYSTEMS RELEVANT TO NUCLEAR SAFETY

Master's thesis for the degree of Master of Science in Technology submitted for inspection, Espoo, 21 May, 2014.

Supervisor **Professor Jari Puttonen**

Instructor **M.Sc. Pekka Välikangas**

Aalto University
School of Engineering

Aalto University,
P.O. BOX 11000, 00076 AALTO
www.aalto.fi

Abstract of master's thesis

Author	Simon Burck
Title of thesis	A method for reviewing structural systems relevant to nuclear safety
Department	Department of Civil and Structural Engineering
Professorship	Structural Engineering and Building Physics
Code of professorship	Rak-43
Thesis supervisor	Professor Jari Puttonen
Thesis advisor(s) / Thesis examiner(s)	M.Sc. Pekka Välikangas
Date	21.05.2014
Number of pages	69 + 5 appendix pages
Language	English

Abstract

The purpose of this thesis to develop a method for focusing the inspection process of design plans of nuclear facilities submitted by nuclear facility license applicants and holders on the most relevant structures and phenomena.

The method consists of a process for creating mathematical models and a spreadsheet tool for running Monte Carlo simulations on the models. The output data is analysed to recognise the most significant parameters affecting the ability of the structure to perform as intended. After the most significant sources of uncertainty have been identified, commissioning of further studies from technical support organisations can be guided using more foreknowledge than was previously possible.

Two case studies were done with goals equivalent to the goals in different phases of the design and inspection process. The first case study is a preliminary investigation of the modellability of a steel-concrete composite structure, which is regarded as an unfamiliar type of structure not covered by the local building codes. The structure, known as an SC-structure, is created on-site by pouring concrete into steel moulds, which remain as part of the composite structure. In accordance with the goals of the inspection process, a relatively detailed mathematical model was created for further study.

The second case study focuses on the parameters affecting prestressing losses in post-tensioned tendons. The methodology was found to be effective in recognising significant parameters and expressing their significance with a concise metric.

Keywords Monte Carlo simulation, SC-structures, Review process, Prestressed tendons

Aalto-yliopisto
Insinööritieteiden
korkeakoulu

Aalto-yliopisto, PL 12100, 00076 AALTO
www.aalto.fi
Diplomityön tiivistelmä

Tekijä Simon Burck		
Työn nimi Toimintatapa ydinturvallisuudelle merkittävien rakennejärjestelmien arvioimiseen		
Laitos Rakennustekniikan laitos		
Professuuri Talonrakennustekniikka		**Professuurikoodi** Rak-43
Työn valvoja Professori Jari Puttonen		
Työn ohjaaja(t)/Työn tarkastaja(t) DI Pekka Välikangas		
Päivämäärä 21.05.2014	**Sivumäärä** 69 + 5 liitesivua	**Kieli** Englanti

Tiivistelmä

Työn tavoitteena on kehittää toimintatapa tarkastusresurssien tehokkaaseen kohdentamiseen olennaisimpiin ilmiöihin ja rakenteisiin ydinlaitosten luvanhaltijoiden rakennesuunnitelmien tarkastuksissa.

Toimintatapaan kuuluu matemaattisten mallien luomista ohjaava prosessi, sekä taulukkolaskentaohjelmassa toimiva Monte Carlo-simulointityökalu luotujen mallien tarkastelua varten. Tulosdataa analysoimalla voidaan tunnistaa merkittävimmät rakenteen toimintakykyyn vaikuttavat parametrit. Kun merkittävimmät parametrit ja ilmiöt tunnetaan, esimerkiksi mahdolliset jatkotutkimukset voidaan tilata teknisiltä tukiorganisaatioilta tarkemmilla lähtötiedoilla.

Tässä työssä on käsitelty kaksi esimerkkitapausta, jotka vastaavat tarkastuksia ydinlaitoksen suunnittelu- ja tarkastusprosessin eri vaiheissa. Ensimmäinen esimerkkitapaus on periaatepäätökseen liittyvän uudentyyppisen, rakennusnormien ulkopuolelle jäävän, teräs-betoni-teräs liittorakenteen tarkastelu. SC-rakenteena tunnettu rakennetyyppi valetaan rakennuspaikalla käyttäen rakenteeseen kuuluvia teräslevyjä valumuotteina. Suunnitteluvaiheen mukainen tavoite on varmistaa rakennetyypin mallinnettavuus tarkempia jatkotutkimuksia varten, mikä myös saavutettiin.

Toinen esimerkkitapaus keskittyy mallinnusparametreihin, jotka vaikuttavat jälkijännitetyissä esijännityskaapeleissa jännityshäviöihin. Menetelmän todettiin soveltuvan hyvin epävarmuuksien löytämiseen ja niiden merkityksen esittämiseen selkeällä mittarilla.

Avainsanat Monte Carlo simulointi, SC-rakenteet, Arviointiprosessi, Esijännitetyt kaapelit

Acknowledgements

Foremost, I wish to express my gratitude to my advisor Mr. Pekka Välikangas, who has enthusiastically provided guidance and a sounding board for bouncing off ideas. My gratitude is also due to my supervisor, professor Jari Puttonen, for his prompt feedback and insightful pointers.

I would also like to thank the National Radiation and Nuclear Safety Authority for commissioning this thesis and Mr. Pertti Pitkänen, who readily shared his expertise, as well as a room at the office, with me. The other structural analysis team members, Messrs. Jukka Myllymäki and Jari Louhivirta also deserve my appreciation for taking the time to answer my seemingly endless stream of questions.

I would also like to thank my girlfriend of many years, Ilona, for putting up with my late nights at the office during the final stages of this work. Last, but not least, a loving thank you to my family for all the support throughout my life.

Table of Contents

List of symbols

Chapter 5

Δ_{error}	Error margin with a 95% confidence interval
$\bar{P}$	Mean sample value
n	Number of samples or iterations
$\mathrm{D}_1, \mathrm{D}_9$	First and ninth deciles

Chapter 6

F	Point load
t_s	Thickness of a steel plate in an SC-structure
B	Distance between studs in an SC-structure
d	Depth of a structure
h_c	Height of the concrete core in an SC-structure
L	Distance between the mid-point of a structure and the supports, or the length of an element
I	Second moment of inertia
A	Cross-sectional area
h	Height of a structure
v	Deflection of a structure
E	Modulus of elasticity
n_s	Number of springs in parallel
k	Spring constant
φ_1, φ_2	Rotations of the beginning and end of a finite element respectively
u_1, u_2	Longitudinal displacement of the beginning and end of a finite element respectively
v_1, v_2	Transverse displacements of the beginning and end of a finite element respectively

M_1, M_2	Moments at the beginning and end of a finite element respectively
U_1, U_2	Normal forces at the beginning and end of a finite element respectively
V_1, V_2	Shear forces at the beginning and end of a finite element respectively
f	Load vector used in the finite element method
u	Displacement vector in the finite element method
K_e	Stiffness matrix of an element in its local coordinates
K_{eg}	Stiffness matrix of an element in global coordinates
T	Transformation matrix
θ	The angle of an element in global coordinates
ε_0	The slip, corresponding to the first turn in the shear force-slip response
Q_u	Ultimate shear strength of a stud
$\mathrm{k_{sec}}$	Secant value of the shear spring constant
Q	Shear force affecting a stud
ε	Slip between the concrete and steel plates in an SC-structure
$\varepsilon_{ct,max}$	Elongation of concrete, at which cracks form
f_{ctm}	Strength of concrete in tension
E_c	Modulus of elasticity of concrete
$h_{c,eff}$	Effective height of the concrete core in an SC-structure after cracking has occurred
w	Deflection of the end of a stud being loaded
Δx	Distance between springs modelling a Winkler foundation
R_j	Reaction force caused by spring number j
d	Diameter of a stud
c	Coefficient of subgrade reaction

w_j	Deflection of the beam at spring number j
L_{stud}	Length of a stud
$M_{reaction,i}$	Internal moment in a beam, at spring j, caused by the springs modelling a Winkler foundation
$M_{bending,i}$	Internal moment in a beam, at spring j, caused by the curvature of the beam
I_{stud}	Second moment of inertia of the beam on the Winkler foundation
M_n	External moment at the end of the beam
F_{cs}	Allowable compression in a steel plate of an SC-structure
ζ_d	Loading time based reduction factor
E_s	Elastic modulus of steel
k_b	Buckling coefficient

Chapter 7

A_c	Cross-sectional area of the wall per a group of three tendons
A_l	Cross-sectional area of the liner
A_s	Cross-sectional area of the reinforcing steel bars
A_p	Cross-sectional area of a tendon
e_{tendon}	Vertical distance between tendons
$\Delta P_\mu(x)$	Friction losses of the tensioning force along a tendon
P_{max}	Tensioning force at the jack
μ	Friction coefficient between the tendon and its sheath or utilisation ratio of the strength of prestressing steel
K	Wobble coefficient
ΔP_{ES}	Loss of tension in a tendon caused by the tensioning of subsequent tendons
j	Coefficient depending on the number of tendons being tensioned
n_t	Number of tendons successively prestressed

$\Delta\sigma_c(t)$	Change in the stress state of the concrete caused by a prestressing tendon
$E_{cm}(t)$	Modulus of elasticity of concrete at the time of tensioning
θ	Cumulative change in angle of the path of a tendon
$\bar{a}, \bar{b}$	Vectors describing the path of a tendon
$\|a\|, \|b\|$	Lengths of vectors describing the path of a tendon
ε_{ca}	Autogenous shrinkage
f_{ck}	Characteristic strength of concrete
$\varepsilon_{cd}(t, t_0)$	Drying shrinkage as a function of age and age, when tensioned
$K(f_{ck})$	Coefficient used in determining drying shrinkage
RH	Relative humidity (in %)
β_{cd}	Coefficient depending on the use of silica in the concrete mix
h_0	Factor related to the exposed surface area and the volume of concrete
$\varepsilon_{cc}(t, t_0)$	Creep of concrete as function of age and age at loading
$\sigma(t_0)$	Stress state in the concrete after tensioning
$\varphi_b(t, t_0)$	Basic creep factor as a function of age and age at loading
$\varphi_d(t, t_0)$	Drying creep factor as a function of age and age at loading
φ_{b0}	Non-time-dependent basic creep factor
φ_{d0}	Non-time-dependent drying creep factor
$f_{cm}(t_0)$	Mean value of concrete cylinder strength at the time of loading
t_d	Age of concrete when drying begins
$\Delta\sigma_{pr}$	Loss of tension in tendons due to relaxation
$\sigma_{pr,i}$	Initial tension in tendons (after instantaneous losses)
f_{pk}	Characteristic value of tensile strength in the prestressing steel

Abbreviations

BWR	Boiling water reactor
COV	Coefficient of variance
EYT	Ei ydinturvallisuusmerkitystä (Non-nuclear related safety class)
ETA	European Technical Approval
FEA	Finite element analysis
FEM	Finite element method
HCLPF	High confidence of low probability of failure
IO	Inspection organisation
LOCA	Loss of coolant accident
MC	Monte Carlo (procedure)
MOE	Modulus of elasticity
NPP	Nuclear power plant
PWR	Pressurised water reactor
RC	Reinforced concrete
RNG	Random number generator
SC	Steel-concrete composite structure
SCi, i=(1, 2, 3)	Safety classes 1 to 3
SSC	Systems, structures and components
STUK	Säteilyturvakeskus (Finnish national Radiation and Nuclear Safety Authority)
TSO	Technical support organisation
VTT	Valtion teknillinen tutkimuskeskus (National technical research centre of Finland)
YVL-Guide	Nuclear power facility related regulatory guide published by STUK

1 Introduction

The current growth in interest in nuclear power plant construction has prompted the commission of this thesis in the Finnish national Radiation and Nuclear Safety Authority, hereinafter referred to as STUK by its Finnish abbreviation. According to IAEA (2014), as of 8.4.2014, there are 72 nuclear power plants under construction worldwide. In Finland, two new construction projects are in the early phases of being approved in addition to one already being constructed.

The purpose of this thesis is to advance the assessment and inspection processes of structural systems. Currently STUK time-consumingly inspects a large amount of detailed plans. This thesis proposes a new framework for reviewing structural systems and stochastically determining critical parameters in the structural systems with the goal of more efficiently allocating resources to the most relevant inspections or sample tests. Any improvement in efficiency is especially welcome, if both planned NPPs go forward.

The next chapter describes the assessment process as it currently is, with sub chapters related to determining the nuclear safety relevance of a structure and the flow of the design process from the point of view of the regulatory body. Chapter 3 discusses how the inspection process can be optimised by using a review methodology based on doing sensitivity and fragility analyses on structures.

Chapter 4 describes the modelling logic and the kinds of structures and questions concerning them that are encountered in the assessment process. The analysis tool is also described. It is a computer spreadsheet, which employs a modular structure for adding new modelling scenarios and a universal module containing the stochastic methodology. Loads and structures are modelled using parameters e.g. pertaining to material properties, geometry and failure modes. The input parameters can be given distributions, which leads to distributions in output parameters. The output parameter distributions are compared to failure criteria, which provide information on the overall margin of safety.

The fifth chapter describes the basic functionality of the modules i.e. spreadsheets that have been created so far. Their inner workings and mathematical basis will be explained at the beginning of each case study.

Two technically very different case studies are presented to evaluate the effectiveness of the method in reviewing structures on an approval-in-principle level. The first, a case utilising the finite element method to model a cross-section of a double skin steel-concrete composite structure, explores the upper limit of the complexity of the calculation modules. The second is a simpler analysis of a post-tensioned tendon in a shell structure using proven equations and actual sample test data from the OL3 project as the basis for material property distributions.

The goals of this thesis are to create a fragility and sensitivity analysis tool to be used by STUK and to accumulate some experience using the new methodology. The tool should be limited to simplistic models to avoid overlap with sophisticated and time-consuming commercial FEM analysis tools and analyses performed by vendors, licensees and their third parties as well as technical support organisations (TSO) consulted by STUK.

2 The current inspection process

This chapter describes the current inspection process in detail. The next sub chapter shows how the inspection work is related to the design process in general and the second sub chapter outlines the basis for recognising the nuclear safety relevance of structures by stating the classification criteria and giving examples of relevant structures.

2.1 The design and inspection process of a nuclear facility

2.1.1 Overview and instances in the design process

Figure 1 depicts the main players and phases of the design process from conceptual design to checking the conformance of a structure to the construction plans. Even though the arrows indicate a linearly progressing process, most of the phases require many cycles of reviews and checks for non-conformances before the actual applications are submitted, which themselves can be subject to review and improvement cycles.

There are four major licensing phases in the design and inspection process of nuclear facilities, with more relating to commissioning and the sub phases in construction. Hold points are points in the design that must be inspected and approved by an inspection organisation before work can continue on the next phases. Hold points are marked with an asterisk symbol (*) in fig 1.

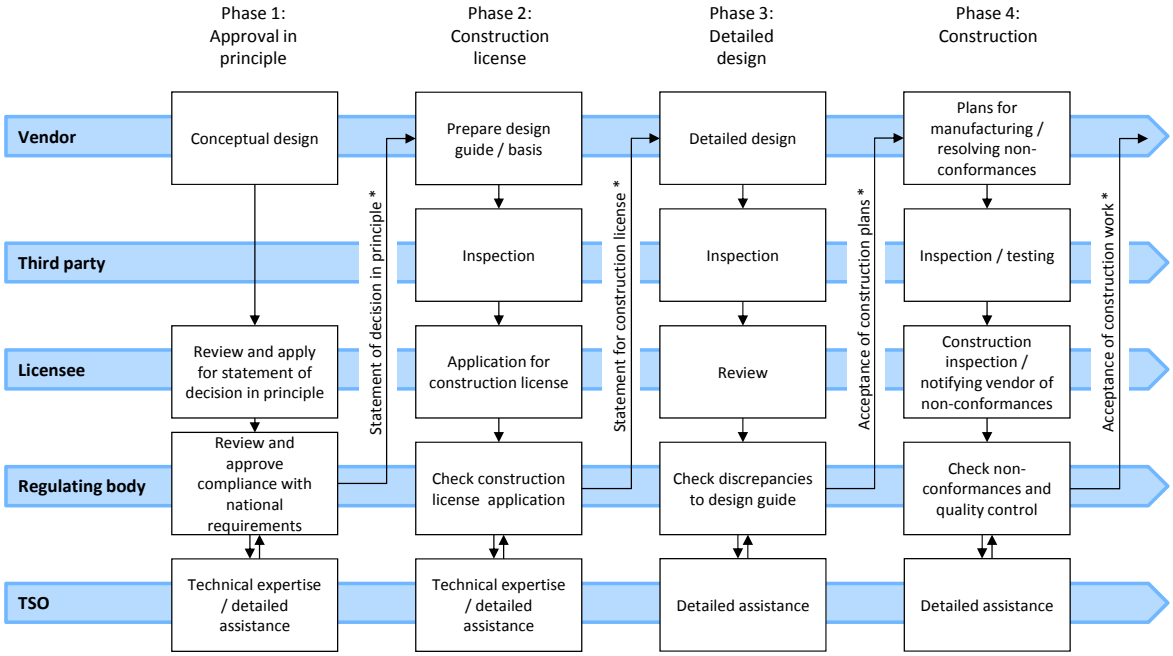

Figure 1. Overview of the design and inspection process up to the acceptance of the construction work.

The different instances involved in the design and inspection process are represented by the horizontal lines in the above figure and their actions in each phase are written in the boxes. The vendor is the company manufacturing and selling the nuclear facility. The licensee applies for the approval in principle, construction license and operating licenses. As the investor and end user of the facility, the licensee takes overall responsibility of the safety and compliance with the regulations. Both the licensee and the vendor use third parties to check and review license applications and design plans, before submitting them to the regulators.

The regulating body in the most important hold points is STUK, but detail inspections and construction related inspections, especially in lower safety classes, can be performed in accredited inspection organisations. STUK uses TSOs like the Technical research centre of Finland (VTT), among others, for their expertise.

2.1.2 Design phases

The four licensing phases related to the design of structures and systems in chronological order are approval in principal, approval of the construction license, approval of the construction plans and approval of the construction work.

The goal of the first phase is to discover any fundamental problems or incompatibilities with the national requirements in the nuclear power plant vendor's conceptual design. The design can already be implemented at another site, but this does not relieve the vendor from any national requirements. The vendor and the license holder review and refine the design to comply with the national standards before

sending it to STUK for approval in principle. Any new structural types are proposed in this phase of the process. STUK can solicit third party statements and analyses regarding any new structural types.

By the end of the first licensing phase, STUK ensures that the structures can be modelled in the subsequent phases and there are no fundamental technical or organisational obstacles to proceeding. After thorough dialog and possible requests of clarification, STUK will issue a nuclear and radiation safety related statement of the decision in principle to the Ministry of Employment and the Economy.

In the second phase, the vendor prepares the design guide, which states the design criteria, including loads, types of structures and standards to be used as the basis for modelling the actions on structures and components and the safety margins of the aforementioned structures and components. It is a prerequisite for the construction license. A third party checks the assumptions and calculations made in the design guide, before the license holder submits an application for a construction license. STUK reviews the design guide with expertise from TSOs, when necessary. In this phase, the review done by STUK is more detailed, because preliminary design parameters are known in more detail. The design guide is revised, if necessary, as part of a favourable statement. The licensee receives the construction license and STUK now has the design criteria against which the subsequent design plans can be checked.

In the third phase, the vendor can finalise the detailed design plans according to the design guide. A third party inspects the detailed design, before the license holder starts submitting the detailed plans to STUK for inspection. STUK's review focuses on checking that the detailed designs are in line with the approved design guide.

In the fourth phase, the vendor and its contractors start constructing the structures according to the design plans. The license holder inspects the construction work and notifies the vendor of any non-conformances. This phase varies in its details depending on the type of structure being constructed. Steel structures and components have sub phases such as shipping and installation, each requiring attention from inspection organisations. Concrete structures' concreting plans as well as pouring readiness are evaluated by inspection organisations before proceeding. The inspection work done in these latter phases often goes unnecessarily far into the details. Development in this area is of primary concern. After the non-conformances are dealt with, STUK can proceed with the commissioning inspection, which can include operating and loading tests.

2.2 Recognizing the relevance of a structural system to nuclear safety

2.2.1 General principles of classification

STUK sets the safety regulations in Finland regarding nuclear energy as mandated by the Nuclear Energy Act (990/1987) § 7 r. These regulations are available in the form of YVL-guides. (Nuclear power facility guides) The third paragraph in the previously mentioned section of the Nuclear Energy Act gives the license holder the option of proposing alternative solutions, which STUK can accept, if they are on par with the required level of safety.

The YVL-guides (STUK, 2013a) define systems as something that contributes to a specific safety or operational function, such as maintaining cooling to the reactor core or containing radioactive substances in the facility in case of an accident. Structures and components are the actual physical manifestations of the system. Every structure and component belongs to a structural system. Systems, structures and components (SSC) are grouped into one of the safety classes, which are from highest to lowest 1, 2, 3 or EYT (classified as non-nuclear). Components and structures are assigned to the safety class of the structural system. Individual components can be assigned to a higher safety class if they border a system of a higher safety class or a lower safety class if they do not affect the accomplishment of a safety function.

A higher safety class leads to higher quality requirements. The requirements focus on ensuring the operation of the safety systems and structural integrity of the structures. The requirements cover design, manufacturing, construction, installation, inspection and operation. The safety classification regarding structures controls attributes such as structural strength, integrity and leak tightness. Components have requirements relating to operational reliability, in addition to the attributes of structures.

Based on the consequences determined by probabilistic risk assessments of a mechanical failure, structures and components are assigned safety classes. Safety class 1 (SC1) is limited to structures and components, whose failure could compromise reactor integrity and require immediate actuation of safety systems. Specifically included in SC1 are the reactor pressure vessel and the components of the primary circuit whose rupture cannot be compensated for by systems used for normal plant operation. Nuclear fuel is also included in this category.

Safety class 2 (SC2) structures and components are those whose: a) integrity is required for reactor decay heat dispersion or containing radioactive substances inside the facility after a SC1 structure or component failure, b) failure enables an uncontrolled chain reaction, c) failure compromises the integrity of nuclear fuel or d) failure compromises the integrity of a class 1 barrier. Some examples of these kinds of structures are core support, reactor shutdown systems' structures, the

containment isolation function and other structures directly connected to the containment.

Safety class 3 (SC3) structures and components are: a) buildings and structures ensuring the operability and physical separation of SC2 systems, b) structures ensuring SC3 functions and c) barriers to the dispersion of radioactive substances and structures where radioactive materials are handled, which are not assigned to a higher safety class.

STUK assesses the appropriateness of the proposed system-level safety classification during the construction license application phase. During the operating license phase, STUK reviews and approves the final safety classification document. Any changes to the classification made in the operational phase of the nuclear facility need to be reviewed and approved.

2.2.2 Examples of safety classified structures

Based on the classification criteria above some structural systems can typically be identified. Nuclear power plants must have a containment, the purpose of which is to contain radioactive substances in the facility after a failure of critical class 1 components. This is sufficient to include it in the SC2 category. Actions assumed to affect the structure in case of LOCA are related to pressure and heat. Integrity is an attribute the structure is designed to maintain. Another related example is the shield building, which protects the inner containment from external threats such as aircraft impacts. It is classified as SC3. For PWR-type NPPs, it is known as an outer containment and for BWR-type NPPs, a reactor building.

Pool structures containing nuclear fuel have high requirements on structural integrity, which in the event of a failure might compromise the integrity of the fuel casings. This justifies including it in SC2. In the long-term, leak-tightness is necessary to prevent gradual spreading of radioactive elements. Pool structures are also subject to requirements concerning load bearing.

Internal structures housing the reactor and other load bearing structures made of reinforced concrete or potentially of steel-concrete-composites (SC) are shown in fig 2. SC-structures are of specific interest, because of their successful use in Japanese NPPs and their unfamiliarity in European design norms. The structures shown in fig 2 vary in their location and purpose in the NPP, which leads to many different safety class designations. Many areas, e.g. those labelled “building” are classified as EYT, are therefore not considered relevant to nuclear safety. The first case study in chapter 5 focuses on SC-structures.

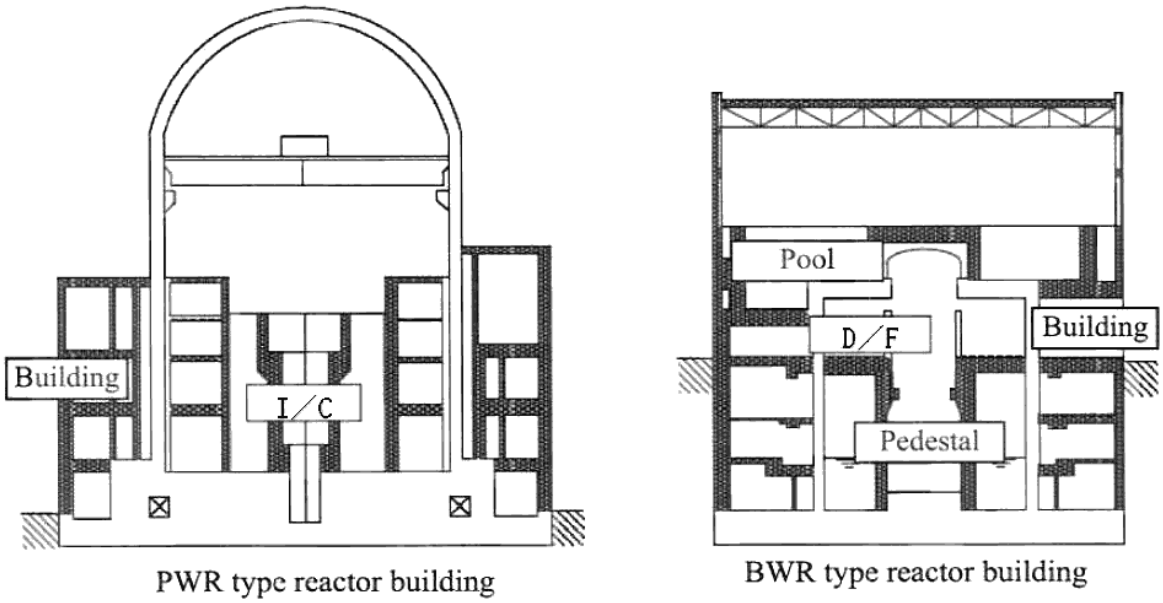

Figure 2. The darkened areas in the figure denote structures potentially made of SC-composites in the two main types of NPPs. I/C stands for internal concrete structure and D/F for diaphragm floor. (JEA, 2010, p. 1.1-2)

The second case study concentrates on the long-term effects on prestressing tendons and the strain state they create. Figures 3 and 4 visualise the hierarchy of real world structures. Some of the most important loads affecting the structures are also shown. In the SSC context, the containment building is part of the containment system and pool structures are part of the radioactive fuel storage systems as well as water storage tanking systems for safety and emergency needs system. Internal structures fall under many different systems.

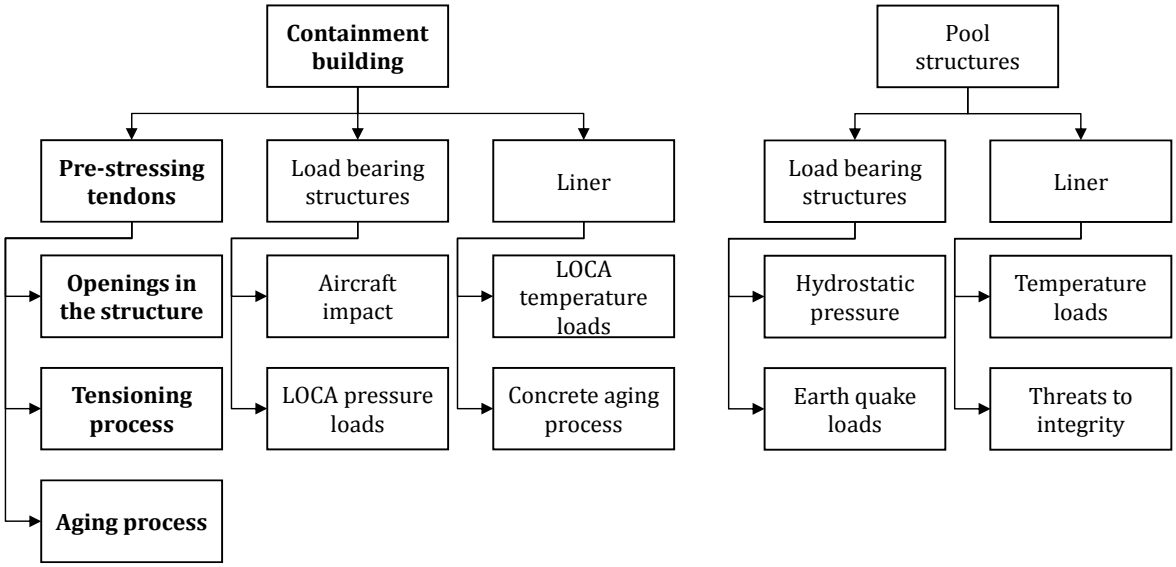

Figure 3. Some examples of structures and the loads and phenomena affecting them. The bolded structures and loads are studied in the second case study.

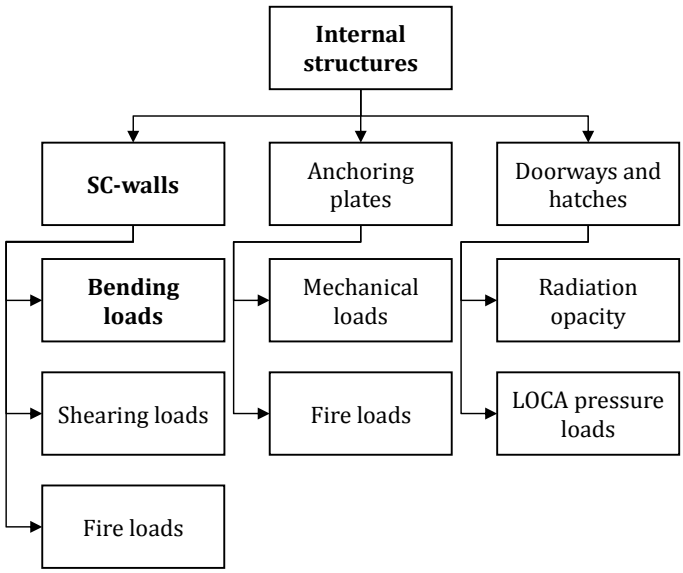

Figure 4. Examples of internal structures and the loads affecting them. The bolded structures and loads are studied in the first case.

3 Development of the inspection process

This chapter describes how the inspection process can be developed by using a simple spreadsheet tool to conduct iteratively improving fragility and sensitivity analyses, the results of which can be used to lower the workload in subsequent inspections. The next sub chapter describes the way the tool is planned to be used in each of the design phases presented in the previous chapter.

The big picture of the design and inspection process, as seen in fig. 1, that describes all the different actors and phases is not changed, but the actions taken in each phase are.

3.1 Using the method in the different design phases

The four inspection phases differ in the goals and the level of detail available regarding the structures. Figure 5 summarises the inspection related actions in each design phase. The steps described below are part of a more rigorous implementation of the so-called graded approach.

The graded approach is a process to ensure that the level of analysis, documentation and actions taken to implement design requirements are commensurate with the relative importance to safety, the magnitude of the consequences of failure, reparability or any other case specific factors. (Agarwal, 2012)

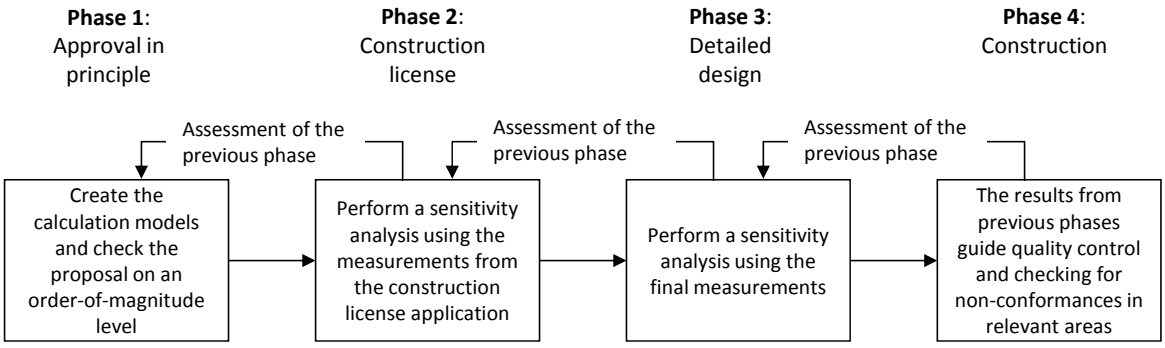

Figure 5. Using the analysis tool in the inspection process. Assessing the previous phase means comparing the design criteria and assumptions to the ones in the previous phase and checking that they are still valid, or that the difference is at least compensated for.

In the first phase of design process, when the vendor is seeking an approval in principle, the regulatory body establishes its first calculation models and assesses their accuracy. Structures and loads are modelled with parameter distributions with high variance, which mirrors the uncertainty and coarseness of the initial plans. The goal in this phase is to acquire a capability to model and analyse the proposed types of structures in more detail in the phases to come. New structural types i.e. those not covered in the building code should be presented in this phase of the design.

In the construction license phase, the design parameters and measurements of structures become more accurate, which enables a proportionally more accurate assessment of the structure. The loads and capacities of the structures are known in more detail. The confidence levels in capacities of the structures rise. Focus in the next phase is determined by the capacity utilisation ratios. A check-back is made to ensure that the proposed design guide is in line with the approval in principle.

Upon evaluating the construction plan in the third phase, the final measurements of the structures are available, which enables the final fragility analyses to be made. This set of calculations also helps assess the accuracy of the earlier design phases.

During the construction phase, the work completed so far is inspected. The higher the confidence level in the calculation methodology and the lower the capacity utilisation ratio or other risks, the less effort can be spent on sample testing the built structures. This being the case, the opposite also holds true. A lower safety class also lessens the need to do sample or spot tests. Capacity utilisation ratio can refer to capacity against the dominant failure mechanism or a combination of the most relevant failure mechanisms.

In general, the variance of the input variables decreases as the design progresses. Initially, even the dimensions of structures may be used as variables, to assess the capabilities of a given type of structure. The first case study is of an approval in principle type analysis, while the second case is more specific, as is the case in an analysis in the construction license phase.

The scope and targets of sample testing depend on the capacity utilisation ratio of the structures and components in question. An acceptable design goal is a high confidence in a low probability of failure (HCLPF). Figure 6 demonstrates the concept of HCLPF.

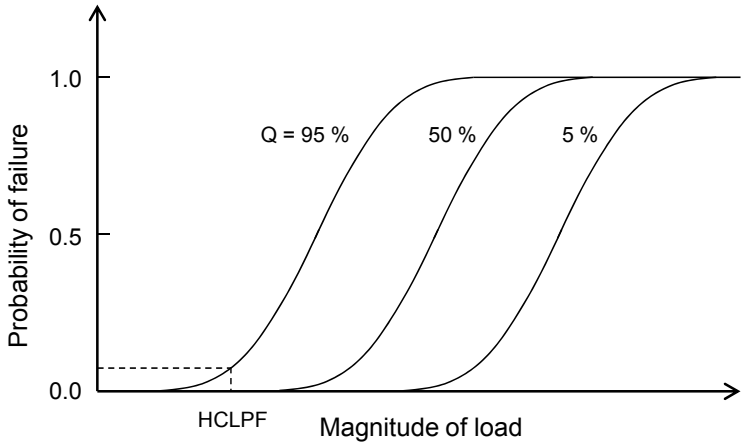

Figure 6. An example of a fragility curve showing a load corresponding to a high confidence in a low probability of failure. Q represents the confidence level of the capacity of the structure against failure.

3.2 The benefits of the method

The sought after benefits of the development are better focused routine inspections and more efficient consulting of TSOs, which is made possible by the deeper understanding of the effects of variation in e.g. dimensioning equations. It is easier to identify the most relevant failure-inducing phenomena.

Instead of checking every detail, inspectors can conduct fragility analyses to determine the critical areas in the structures and concentrate inspections on them. Discussions with employees doing inspection work, presented the possibility that using the tool would make the inspection more analytical and therefore more intellectually engaging. This could lead to higher job satisfaction in addition to the expected timesavings.

4 The review method

This chapter describes the analysis tool and the creation of the calculation models used by it. The analysis tool is based on a computer spreadsheet, which has automated functions for inputting parameters with a definable distribution to a calculation model and for saving the corresponding results. Relationships between the input and the results can be identified from a large number of input-result pairs. The calculation models are case-specific and must be created for each type of structure and sometimes even loading type.

The output variable distributions are compared to failure criteria, which provide information on the overall margin of safety. The failure criteria can themselves depend on the input variables e.g. material properties. However, not all simulations aim to determine a failure mode. In the tendon case, variations in the prestressing losses are themselves the desired result.

4.1 The modelling process of a structural system

There are five steps in the modelling process of a structural system. The steps are named in fig. 7.

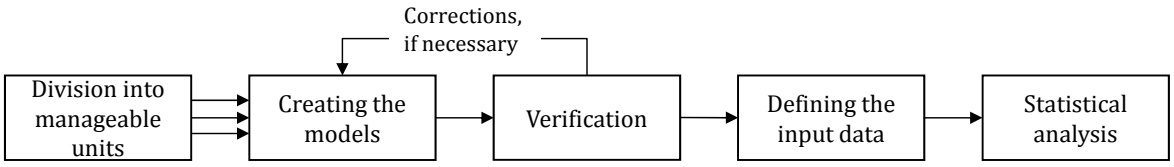

Figure 7. The necessary phases in creating and using a model.

Reviewing a structural system begins by dividing it into manageable pieces, that can be modelled using simple spreadsheet sized calculations. Structural systems are broken down into components and structures, which are analysed for failure mechanisms or other phenomena. Other phenomena are explicitly mentioned to avoid limiting the applicability of the tool. Figure 8 depicts the breakdown of systems into modellable problems.

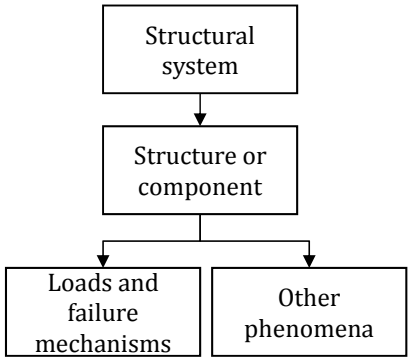

Figure 8. Division of the structural system into modelling scenarios.

For example, the concrete in the inner containment building should generally be in compression. This includes situations due to e.g. aging, loads and the environment. Many questions arise from this premise. What is the magnitude of prestressing losses due to aging effects? In what bounds does the prestressing force in the tendons change due to aging? How is leak-tightness of the liner affected by accident loads and aging effects? Prestressing losses have been selected to be analysed in the second case study.

The YVL guide E.6 (STUK, 2013b) section 6.4 states that once a specific scenario has been defined and the relevant physical phenomena are identified, calculation models can be made using widely accepted methods given e.g. in standards or design codes.

The verification of the calculation models used to check design calculations and help guide inspections does not need to be as stringent as the verification of the actual design models, though similar principles apply. The YVL guide E.6 requires that design models be verified with simpler calculations and that the specific version of a complex e.g. FEA-based program used in the calculations is validated.

4.1.1 Creating the models

Creating a module begins with a worksheet, which contains the calculations necessary to assess the phenomenon in question. A module may contain many models e.g. material models. The overall calculation model may consist of many interconnected modules. The typical structure of a calculation model is summarised in fig. 9. Having separate sub modules is optional, but the other parts are necessary for the methodology.

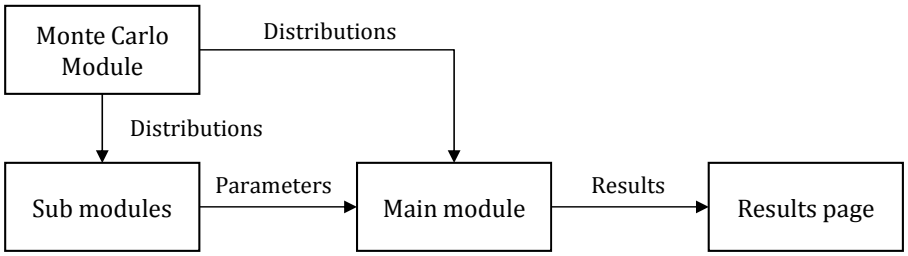

Figure 9. The relationship of the different modules. Arrows indicate data flow between the modules. The result page can be considered a part of the Monte Carlo module.

The line between including some part of the calculation in the main module and creating a sub module for it is arbitrary, but some suggestions can be made. If the calculation is resource intensive and is not required to be recalculated for each round of the simulation, having it in a separate module can reduce the simulation time. Another reason to create a sub module is to make it easily available for future calculation models. On the other hand, modelling experience has shown that, additional worksheets complicate mitigating Excel's tendency to recalculate whole

worksheets unnecessarily leading to slower calculation times. After creating the calculation modules, the Monte Carlo module is added to the workbook as a separate worksheet.

The modules used in the calculation model for analysing an SC-wall include a sub module for calculating the stiffness of the studs. This information becomes a parameter among many others in the main module, which employs material models and the Finite element method for the so-called truss model. The Monte Carlo module performs repetitive calculations using the truss model with different input parameters each time to produce distributions of the chosen result variables.

4.1.2 Verification

Any new models or equations must be compared to empirical tests or reliable existing models. If no relevant empirical data is available, STUK can request that the licensee conduct experiments to back up the used calculation models or material properties therein. For example, in the second case study pertaining to the prestressing tendons in the containment building, the relaxation parameter used in the models was backed up by experimental tests.

The first Monte Carlo runs can be used for self-verification by checking for unexpected relationships between input and output variables. This might uncover errors in the model or interesting non-obvious relationships. Some input variables might have a negligible effect on the results and can therefore be excluded from the model or set as a constant instead of being given a distribution. The choice of using a spreadsheet based tool was partly motivated by the fact that a spreadsheet has all the information contained in it in an easily accessible form, which makes it more easily verifiable.

4.1.3 Defining the input parameters

Defining the distributions of the input parameters to be representative of the underlying physical phenomena is as important as having an accurate calculation model. Ideally, all the parameters' distributions would be based on empirical evidence, but in reality, estimates and simplifications have to be made. However, NPPs require such high levels of certainty, that effort can be spent e.g. to monitor the properties of each batch of concrete used at construction site. YVL E.6 states that "any significant design parameters not based on standards must be empirically proven." This creates a great source of data to be used in calculations.

4.2 Analysis

4.2.1 Analysing the results

The tools in the Monte Carlo module offer ways to quickly view scatter plots of the input variables against the result variables. This allows regression analysis using

the built-in tools of the spreadsheet program. Many different regression models are available from a simple linear fit to polynomial and exponential fits.

A proper analysis requires a significant number of iterations to reduce the effects random noise. Experiences using the tool have shown the number to be in the thousands. The relationships found in the verification phase can now be confirmed with higher certainty. Non-linear relationships are of particular interest.

If failure data exists, it can be compared to simulated loading data to estimate a probability of failure as a function of loading to create a fragility curve. If failure data for a component or structure is not readily available, it can be modelled using e.g. material and geometry related parameters, whose uncertainty is modelled with distributions with an appropriate variance.

4.2.2 Using the results of the analysis in practise

Potential applications of the methodology are shown in figs. 3 and 4, which depict typical systems and structures inspected by STUK. As an example, pool structures could be analysed under thermal loads. Pool structures are concrete structures lined with a thin sheet of steel held in place by studs to ensure leak-tightness. Temperature changes cause strains through thermal expansion.

The results of an analysis could e.g. show that out-of-straightness is not a crucial factor in the failure mechanisms of a structure. This information could be directly used in the construction phase to reduce the effort used checking the structure for errors in construction tolerances.

5 Calculation modules

This chapter describes the calculation modules created so far. The most important module is the Monte Carlo module, because it is necessary for the methodology. The other modules are case specific, like the stud module, which is used to calculate the effects of shear forces affecting studs embedded in concrete. The tendon module is also very specific in its uses. However, the module based on the finite element method could eventually become a general-purpose module.

5.1 The Monte Carlo module

Monte Carlo simulation is a broad range of techniques to approximate solutions to quantitative problems using statistical sampling. In this thesis, the focus is on translating uncertainties in input variables into uncertainties in the output variables by using a calculation model as summarised in fig. 10.

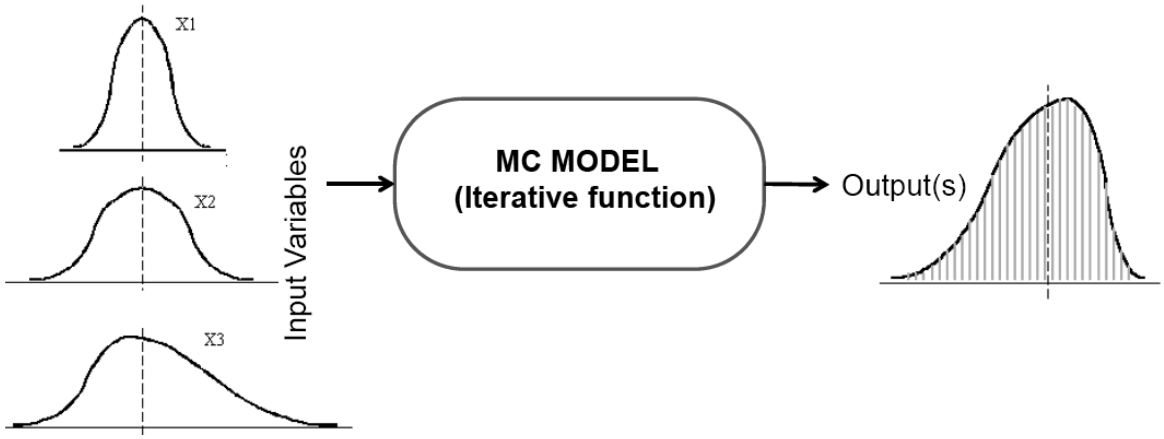

Figure 10. Relationship between the density functions of input variables and the density function of an output distribution. (Mazaheri, 2013)

5.1.1 Monte Carlo process

To set up a Monte Carlo simulation, three conditions have to be met. A calculation model needs to be defined, variable parameters and their distributions have to be defined and a termination condition has to be established. The termination condition can be a specified number of iterations, a time limit or, more generally, a target function, whose convergence is the trigger for the end of the iteration. Some simple target functions could be the difference between the mean values and variance of the probability functions and generated values of input parameters.

The Monte Carlo process has four steps, which are in operational order: generate parameter values from defined distributions, evaluate the calculation model, save the results and start again if the termination condition has not been met. Figure 11 contains the complete process chart.

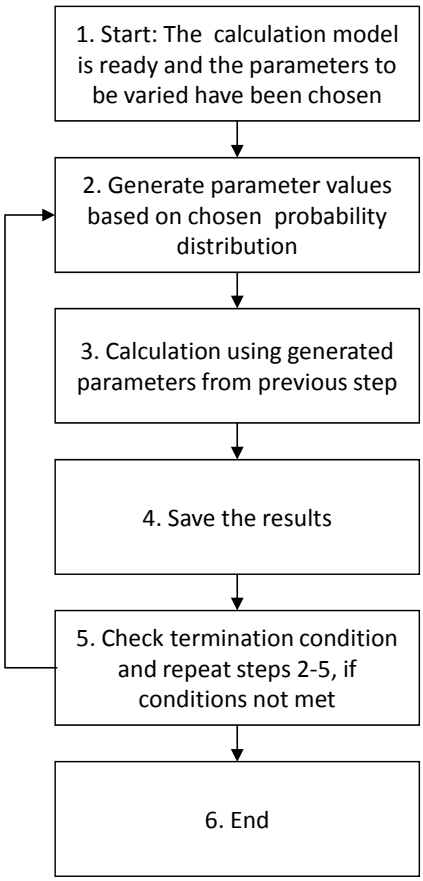

Figure 11. The Monte-Carlo process chart.

5.1.2 Description of the Monte Carlo implementation

The Monte Carlo module consists of two worksheets. The first is the input page, which defines the termination conditions for the iteration and the variables to be used in the calculations. The second page holds the results of the calculations and some rudimentary analysis tools to help understand the relationship of the input variables and the output variables. Figures 12 and 13 are screen captures of the input page and the results page respectively. Key areas are numbered for easier referencing.

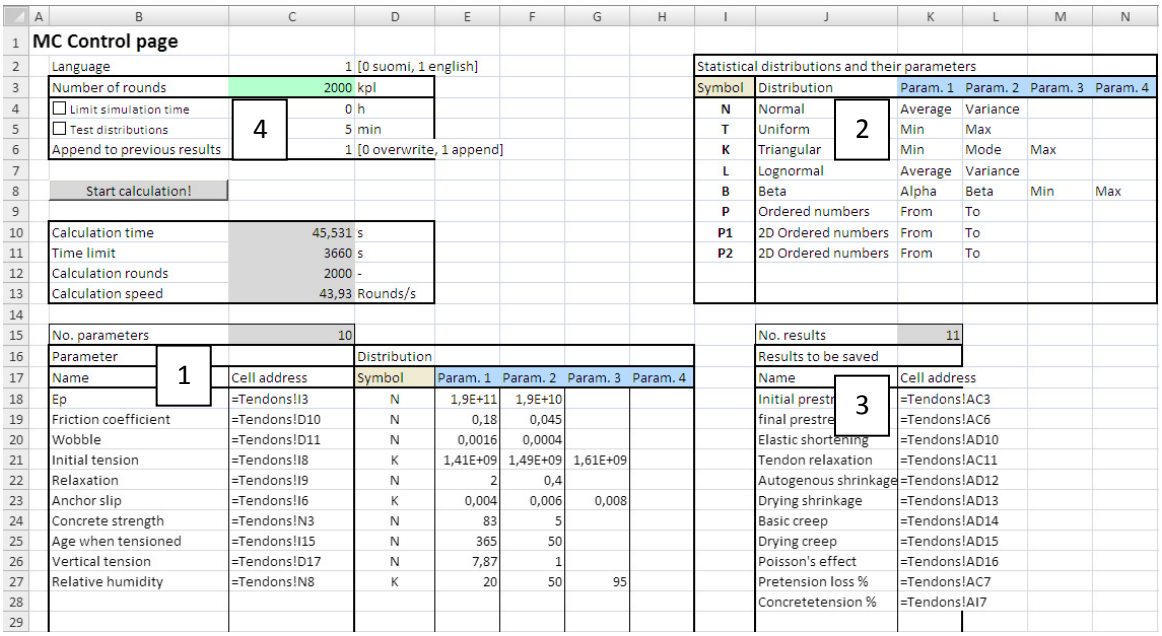

MC Control page

Language	1 [0 suomi, 1 english]
Number of rounds	2000 kpl
Limit simulation time	0 h
Test distributions	5 min
Append to previous results	1 [0 overwrite, 1 append]

4

Start calculation!

Calculation time	45,531	s
Time limit	3660	s
Calculation rounds	2000	-
Calculation speed	43,93	Rounds/s

Statistical distributions and their parameters

2

Symbol	Distribution	Param. 1	Param. 2	Param. 3	Param. 4
N	Normal	Average	Variance		
T	Uniform	Min	Max		
K	Triangular	Min	Mode	Max	
L	Lognormal	Average	Variance		
B	Beta	Alpha	Beta	Min	Max
P	Ordered numbers	From	To		
P1	2D Ordered numbers	From	To		
P2	2D Ordered numbers	From	To		

No. parameters: 10

1

Parameter		Distribution				
Name	Cell address	Symbol	Param. 1	Param. 2	Param. 3	Param. 4
Ep	=Tendons!I3	N	1,9E+11	1,9E+10		
Friction coefficient	=Tendons!D10	N	0,18	0,045		
Wobble	=Tendons!D11	N	0,0016	0,0004		
Initial tension	=Tendons!I8	K	1,41E+09	1,49E+09	1,61E+09	
Relaxation	=Tendons!I9	N	2	0,4		
Anchor slip	=Tendons!I6	K	0,004	0,006	0,008	
Concrete strength	=Tendons!N3	N	83	5		
Age when tensioned	=Tendons!I15	N	365	50		
Vertical tension	=Tendons!D17	N	7,87	1		
Relative humidity	=Tendons!N8	K	20	50	95	

No. results: 11

Results to be saved

3

Name	Cell address
Initial prestr	=Tendons!AC3
final prestre	=Tendons!AC6
Elastic shortening	=Tendons!AD10
Tendon relaxation	=Tendons!AC11
Autogenous shrinkage	=Tendons!AD12
Drying shrinkage	=Tendons!AD13
Basic creep	=Tendons!AD14
Drying creep	=Tendons!AD15
Poisson's effect	=Tendons!AD16
Pretension loss %	=Tendons!AC7
Concretetension %	=Tendons!AI7

Figure 12. A screen capture of the Monte Carlo control page with numbered areas whose functions are explained below.

Area 1 specifies the parameters that are to be varied. In the first column, a name can be given to variable. The name should be distinct, because it is the only way to identify the generated data later on in the analysis. Next, the address of the cell containing the variable used in the calculation is specified in the next column. To select the address the ”=” sign is typed in and the cell can be selected using the pointer. The column properties have been modified to show the address of a cell, not its value. The next column specifies the kind of distribution of the values to be generated for the selected parameter. The next columns are reserved for the parameters needed to define the distribution.

Area 2 lists the possible symbols to be used to define distributions and the parameters needed to define the distributions. The available distributions are normal, uniform, triangular, lognormal and beta. Non-random, sequential numbers can be used as input.

The third area is used to define the results that are saved after each iteration of the calculation. The first column names the variable and the second is the address of the cell containing it.

Finally, area 4 contains the data for controlling the number of iterations. The number of iterations can be defined and a time limit can be specified. Which ever is met first will stop the iteration process.

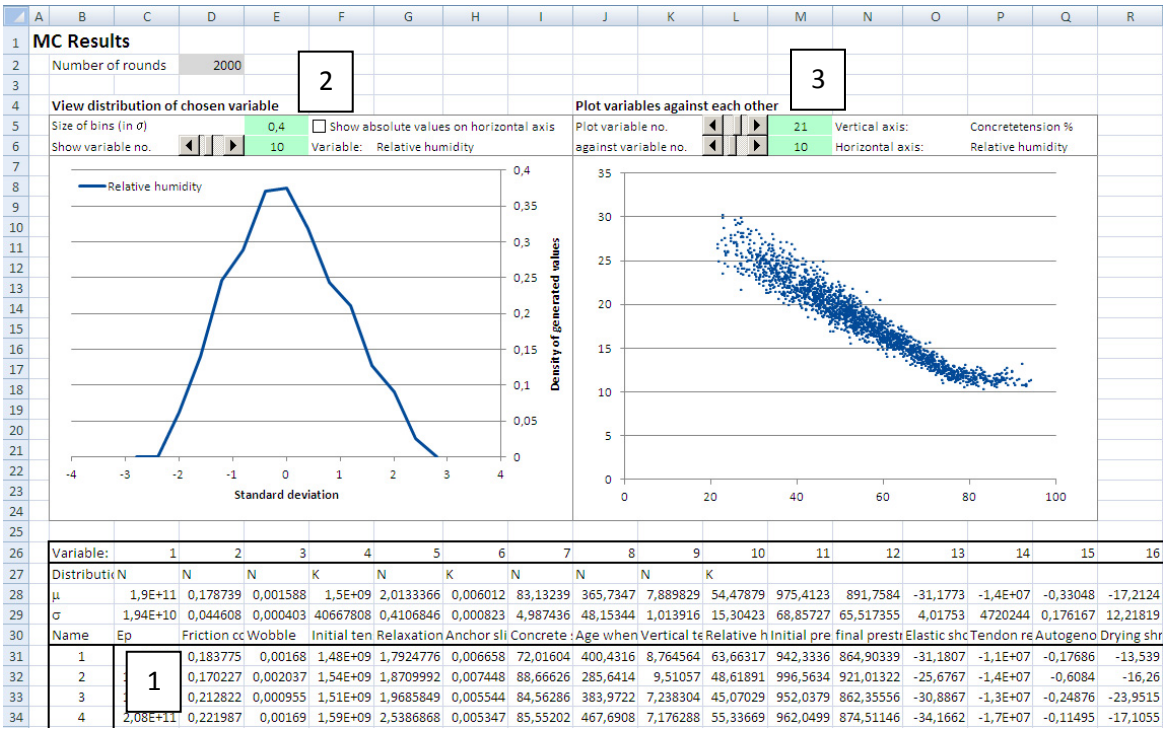

Figure 13. The Monte Carlo results page. The numbered areas are explained below.

Area 1 contains the names of the variable on row 30. Each row down contains the values of the variables from one iteration of the calculation. The rows above the name contain the standard deviation and mean values of the variable in question. For input parameters, the next row up shows the distribution type used to generate the values of the parameter. For output or result values, the distribution row is empty. Finally, the “variable” named row numbers the columns of values, so that they can be easily referenced when analysing the data.

Area 2 displays a graphical representation of the distributions of the chosen variable. It can be used to check that the generated variable distributions are as expected or how the output variables are distributed. The displayed variable can be chosen by changing the number next to the cell labelled “show variable no.” to the corresponding one on row 26. The density function can be plotted as a function of absolute values or standard deviations. The distribution seen as an example is derived from a triangular source distribution.

The third area is used to plot variables against each other. The variables to be plotted can be changed using the sliders or by directly typing in the number of the variable. Built-in tools like the trendline function are helpful in determining the relationship of the variables. The example plot is of relative humidity and its effect on the loss of prestress in the concrete as will be described in the second case in chapter 7.

To quantify the effects of each variable, an indicator was created. It is calculated using the difference between two points on the trendline function. The points correspond to the first decile and the ninth decile of the input variable. The non-normalised significance of an input variable can be calculated as follows:

$$\text{Significance}_{0,\text{i}} = \text{abs}[\text{trendline}(\text{D}_1) - \text{trendline}(\text{D}_9)], \quad (1)$$

where D_1 is the first decile of the input variable, D_9 is ninth decile, trendline() is the appropriate function to describe the data and abs() converts values to absolute values so that negative and positive correlation are treated equally. Finally, the values are normalised by dividing all the calculated non-normalised significance values with the one with highest value.

$$\text{Significance}_{\text{i}} = \frac{\text{Significance}_{0,\text{i}}}{\text{Significance}_{\text{max}}}, \quad (2)$$

This method assigns the highest value to variables with a combination of a high coefficient of variance and a high gradient in the result function. Additional attention should be given to regression curves that their extreme value between the beginning and final values as shown in figure 2 in appendix 3.

5.1.3 Randomness of the generated numbers

The Monte Carlo method relies on the randomness of the generated numbers. There has been some doubt (McCullough, 2008) about the effectiveness of Excel's built-in random number generator (RNG). Therefore, in the spirit of verifying all used tools, a quick test of Excel's RNG was performed.

The documentation to the function "Rand()" claims that it produces evenly distributed random numbers between 0 and 1. The Monte Carlo method can be used to calculate π by comparing the areas of a circle touching all sides of a square. These areas can be approximated by sprinkling points onto area and counting how many are inside the circle. As the number of sprinkled points increases, the ratio of points inside the circle to all points will converge to $\pi/4$, if the points are randomly distributed.

The results in figure 14 confirm that the RNG is at least good enough for our purposes. The approximation of π converges to the correct value. The value of π is approximated within the expected error margin, Δ_{error}, (in %) with an confidence interval of 95% given by

$$\Delta_{\text{error}} = 200\sqrt{\frac{1-\bar{P}}{n\bar{P}}}, \tag{3}$$

where n is the number of randomly generated points and $\bar{P}$ is mean sample value, which is expected to be π/4 in this case. (Ang & Tang, 2007, p. 201)

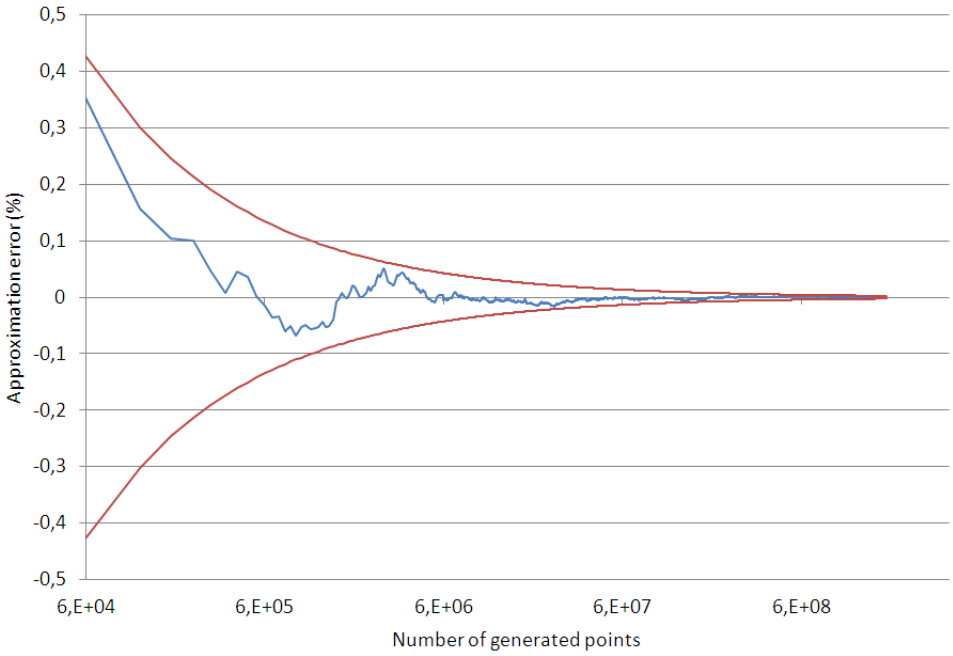

Figure 14. The approximation error (in blue) and the error margin with (in red) as a function of the number of iterations.

As seen in fig. 14 the solution converges as expected. However, this demonstration serves only as a quick and low certainty verification of the used method, not an absolute proof.

5.2 Case specific modules

Other modules created for the case studies include a FEM-module, for modelling structures and loads affecting them, a stud module, which models how a stud behaves in concrete and a tendon module, which models the effects of aging on tendons and the tendon's deviation from a plane due to obstacles.

The verification of the models in these modules will be presented as part of the case studies in which they are used.

5.2.1 The FEM module

The FEM module calculates the effects of physical loads on structures that can be represented by interconnected beams. These effects include strains, displacements and the internal forces of the structure.

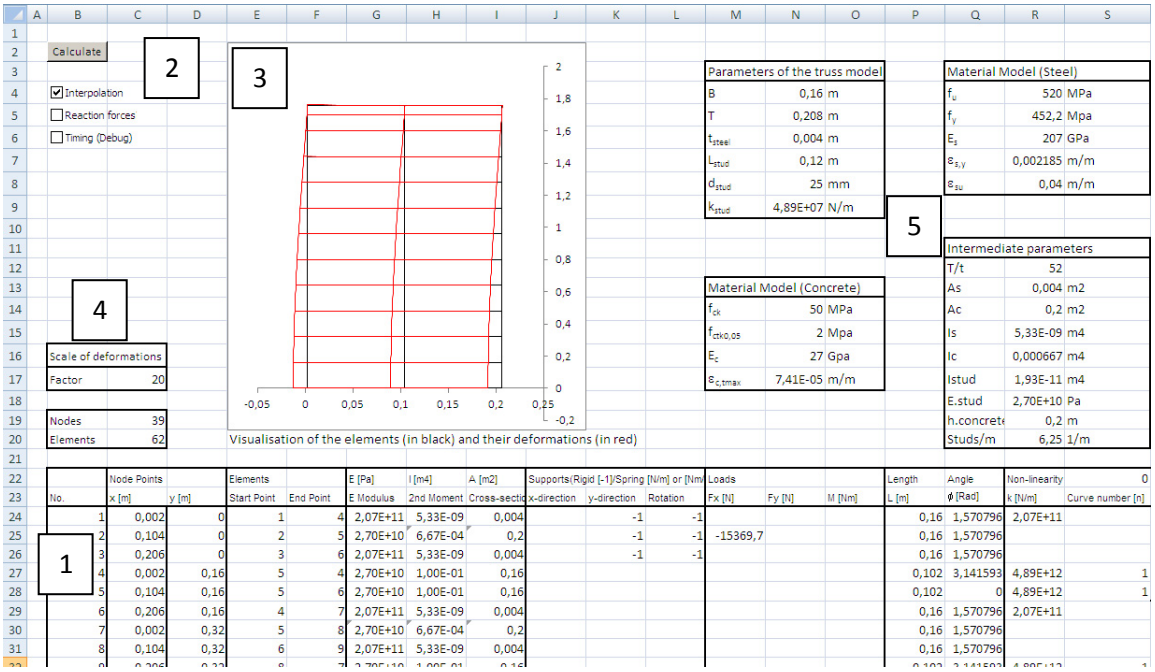

No.	Node Points x [m]	y [m]	Elements Start Point	End Point	E [Pa] E Modulus	I [m4] 2nd Moment	A [m2] Cross-sectio	Supports(Rigid [-1]/Spring [N/m] or [Nm] x-direction	y-direction	Rotation	Loads Fx [N]	Fy [N]	M [Nm]	Length L [m]	Angle ϕ [Rad]	Non-linearity k [N/m]	0 Curve number [n]
1	0,002	0	1	4	2,07E+11	5,33E-09	0,004		-1	-1				0,16	1,570796	2,07E+11	
2	0,104	0	2	5	2,70E+10	6,67E-04	0,2		-1	-1	-15369,7			0,16	1,570796		
3	0,206	0	3	6	2,07E+11	5,33E-09	0,004		-1	-1				0,16	1,570796		
4	0,002	0,16	5	4	2,70E+10	1,00E-01	0,16							0,102	3,141593	4,89E+12	1
5	0,104	0,16	5	6	2,70E+10	1,00E-01	0,16							0,102	0	4,89E+12	1
6	0,206	0,16	4	7	2,07E+11	5,33E-09	0,004							0,16	1,570796	2,07E+11	
7	0,002	0,32	5	8	2,70E+10	6,67E-04	0,2							0,16	1,570796		
8	0,104	0,32	6	9	2,07E+11	5,33E-09	0,004							0,16	1,570796		

Figure 15. Input page for the FEM module.

The first numbered area in fig. 15 contains the information needed to define the elements used by the finite element method. The first column, B, contains a running number used to reference node points and elements. The next two columns define the coordinates of a node point in a two dimensional plane. The positive directions are to the right and up. Cells C24 and D24 define a node whose reference number is in cell B24 i.e. 1. C25 and D25 correspond to the reference number in cell B25, and so on. Once enough nodes have been defined, elements are defined by selecting two nodes to be connected. Columns E and F are filled with the reference numbers of nodes to define the starting and ending points of an element. The chart in area 3 visualises the elements as they are drawn and is a good way to ensure that the structure is input as intended.

Columns G to I contain the properties of the beam element. The necessary properties for beam elements are modulus of elasticity, second moment of inertia and cross-sectional area. The number of properties should be equal to the number of defined elements, because an empty cell will be interpreted as zero. This will cause the calculation to fail when inverting the stiffness matrix. The program helps the user by automatically highlighting the proper amount of rows to be filled.

Next, the desired boundary conditions, that restrict movement of node points, are filled into the next J, K and L columns. Each row corresponds to the node that was defined on the same row. The user can specify a spring constant that restricts the movement of the node by typing in a positive number, or a rigid support that prevents movement altogether by typing in the value “-1”. The First column defines boundary conditions in the horizontal direction, the second in the vertical direction, and the third against rotation. No assumptions about the units are hardcoded into the program, so the user is free to use any desired units as long as no unit conversion is expected from the program. The base units used for testing were N and m.

Finally, the loads affecting the structure are added. Loads can only interact with the structure at node points. The columns M, N and O correspond to loads in the horizontal direction, vertical direction and moments. As with the boundary conditions, the row the loads are typed into correspond with the node defined on that row. The positive direction of the loads is the same as with the coordinates and, for moments, a positive value signifies a clockwise-directed moment. The next columns display the lengths and angles of the elements calculated by the program, so that the user can check for errors in the input data.

After the input data is filled in, the calculation can be initiated from the calculate button in area 2. Pressing the button runs a macro that creates the stiffness matrix and inverts it using macros written in visual basic and worksheet functions. Other options are available below the button, e.g. turning on and off interpolation of the deformed structure, timing the calculation for debugging purposes and calculation of reaction forces.

Now the actual calculation is finished and the results i.e. the deformation of the structure can be drawn. The deformed structure is superimposed on the initial structure in area 3. The deformations are interpolated for the visualisation to better visualise the rotations of the beam elements. The interpolation algorithm is explained in appendix 2. The scale of the deformations can be magnified by changing the scale factor in area 4. Manually clicking the button to calculate the results is only done when building and testing the model. During the actual Monte Carlo simulation, the calculation is initiated automatically for each round.

Area 5 contains parameters that control the input data described above. For example, the thickness of the structure being analysed can be changed by a single parameter that controls the coordinates and cross-sections of the elements. The description of the methods and equations used in the module is in the chapter describing the case study of the SC-structures.

5.2.2 The stud module

The stud module is a used as a sub module in the SC-structure case. Its purpose is to model the interactions of a stud holding the steel plate together with the concrete core. Specifically of interest is the relationship between shear force and slip between the steel and concrete. The model is based on a beam on a bed of springs also known as a Winkler foundation.

Figure 16 shows the input parameters in area 1 and the way it visualises the displacements caused by a transverse force at the end of the beam in area 2. The third area holds the result of the calculation i.e. the spring coefficient describing the shear-slip ratio. Again, the equations and model behind the module are described in the first case study.

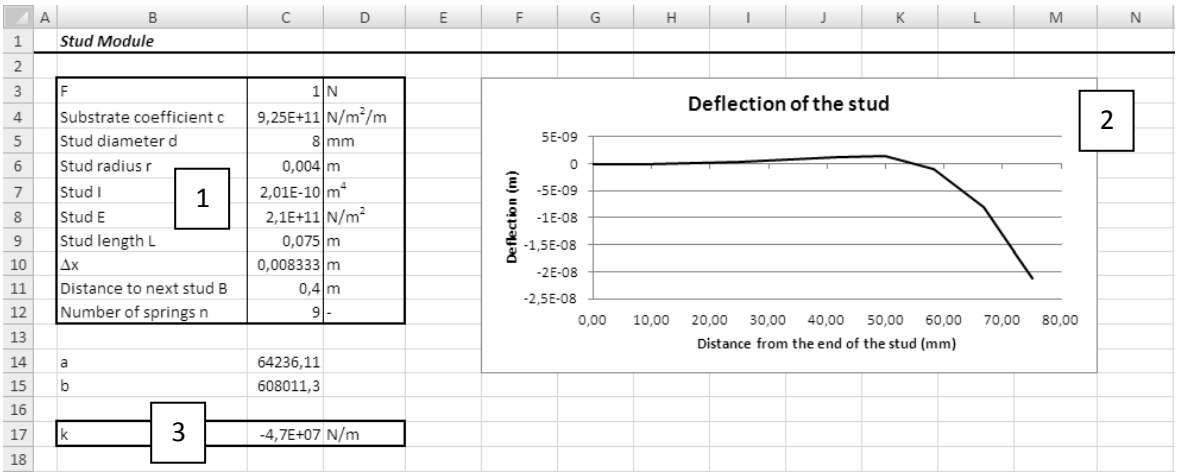

Figure 16. A screen capture of the stud module.

5.2.3 The tendon module

The tendon module calculates the stress-states of different constituent parts of a containment building's wall structure. The parts included in the model are the liner, reinforcement bars, concrete and prestressing tendons. A illustration of the cross-section is presented in the case study in fig. 39. Figure 17 shows the input area of the tendon module, which contains all the parameters controlling the model. At the bottom of the figure, there are charts that help the user to verify that the geometry of the problem was input as intended. Other instantaneous sources of visual feedback are the charts representing the calculated tension in the tendons and the cumulative change in angle along the tendon, which is a major parameter pertaining to friction-induced losses.

The main categories of input parameters are related to the geometry and properties of a tendon, concrete properties, the geometry and reinforcement of the wall structure and the transverse compression state.

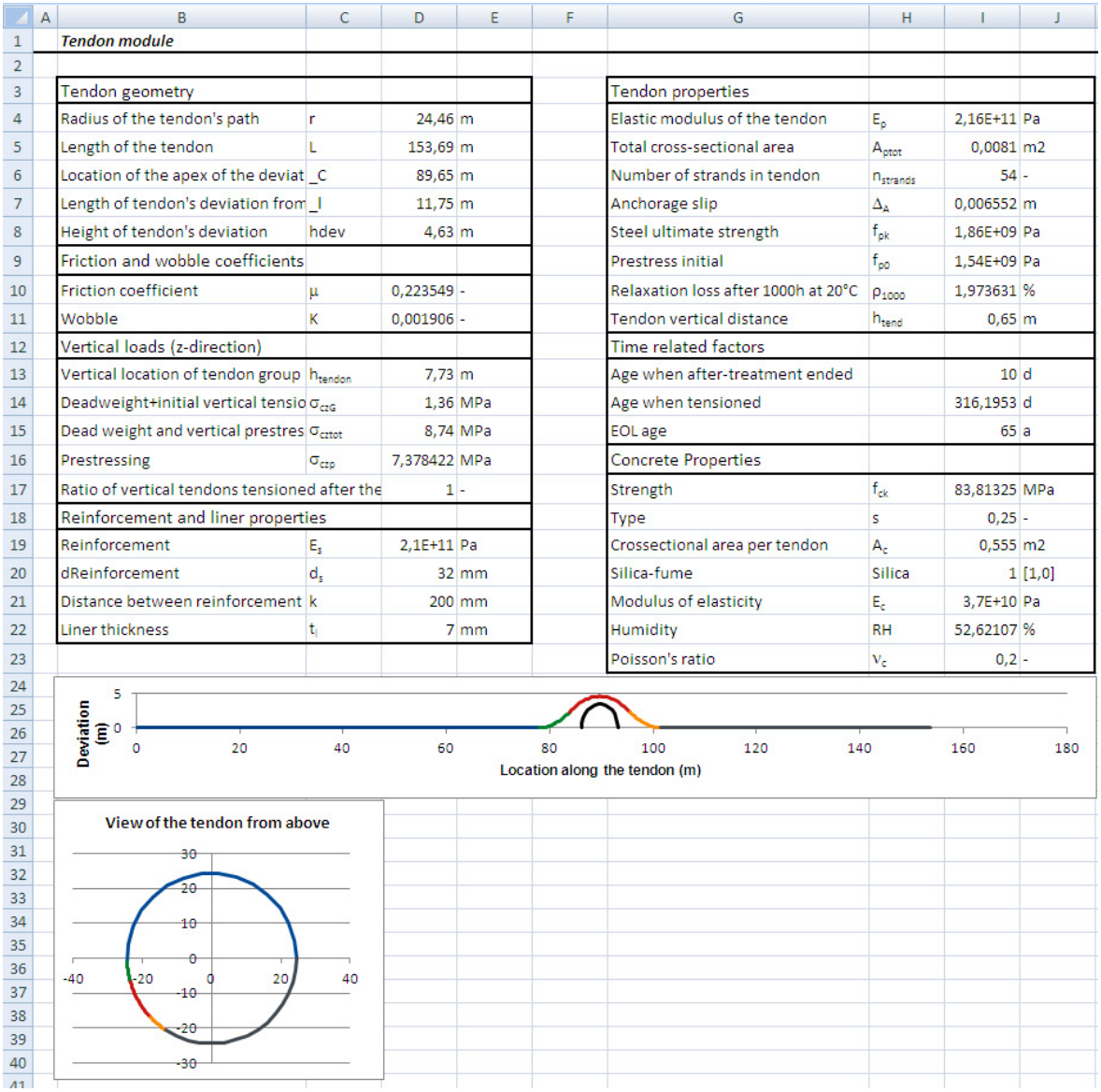

Figure 17. Screenshot of the input area of the tendon module.

6 Case 1: Bending an SC-structure

In anticipation of nuclear power plant vendors' new structural designs, SC-structures were chosen for an approval-in-principle level investigation. The goal is to see if SC-structures can be simply modelled in-house at STUK and establish a baseline understanding in this type of structure. This study concentrates on modelling the studs and the forces and deformations affecting them.

Three different steel plate-structure thickness ratios are compared. A Japanese design code, JEAC-4618:2008, is used as a guide to define realistic geometrical parameters for the SC-structures, because the Eurocodes do not yet include design standards for them. The parameters derived from the Japanese standard are the distance between studs, steel plate-structure thickness ratio and maximum stud size.

6.1 A brief description of SC-structures

An SC-structure is a composite structure with a concrete core and steel plates on either side of it. A half SC-structure has a steel plate on one side and reinforcement bars on the other. The steel plates are attached to the concrete using shear studs. Figure 18 shows a plate with welded studs being constructed.

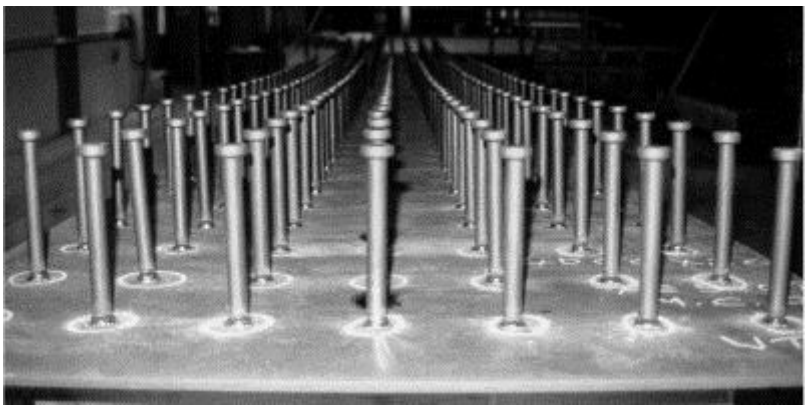

Figure 18. Shear studs welded to a steel plate. (McKinley et al, 2002 p. 1349)

The steel plates are used as a permanent mould for the concrete. The advantage to this type of structure is that the amount of work done at the construction site is smaller than traditional reinforced concrete structures. Figure 19 depicts an idealized cross-section of an SC-wall. Shear studs protrude into the concrete and tie-bars hold the plates in place against the hydrostatic pressure and vibration during the pouring of the concrete. Tie bars will not be accounted for in the model.

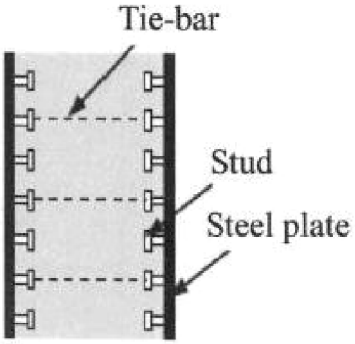

Figure 19. A cross-section of an SC-structure. (JEA, 2010 p. 1.1-4)

6.2 Overview of the modelling logic

The effects of bending on an SC-structure are investigated in simulated a three point bending experiment as shown in fig. 20. This loading situation was chosen, because the results can be directly compared to peer-reviewed experimental results by McKinley et al. (2002). In the experiment, an SC-structure was loaded until failure and the deflection was measured. The goal is to first replicate the experimental results and then analyse different ratios of structure thickness and steel plate thicknesses using the newly created model.

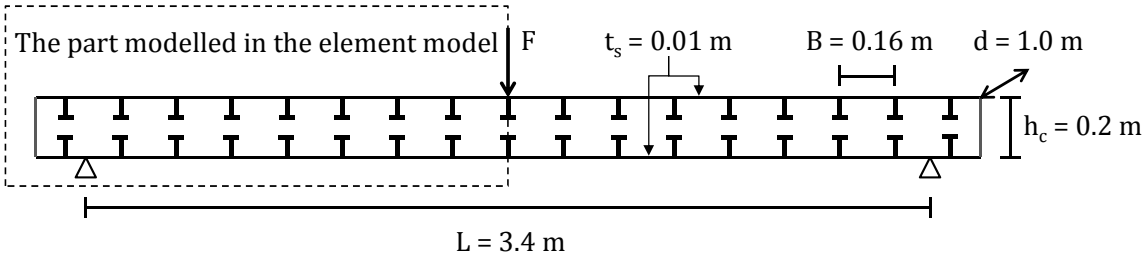

Figure 20. The dimensions, supports and loading of an SC-structure in a three point bending experiment.

Due to symmetry, only half of the structure must be modelled. The finite element model representing the dashed area is illustrated in fig. 21. The depth of the structure, d, is 1.0 m and the thickness of the steel plates, t_s, is 10 mm. The studs are spaced 0.16 m apart in the depth direction as well as along the wall.

Using the modelling logic described in fig. 9 in chapter 4, the main module is the FEM-module. A model consisting of a configuration of elements illustrated in fig. 21 called an element model is created. Some elements receive special properties calculated in a sub module, i.e. the stud module. The border conditions reflect the line of symmetry in the middle of the structure. The right side of the element net has supports that are fixed against rotation and horizontal movement, but not vertical movement. The support at the bottom-left only prevents vertical displacement. The elements are modelled as being on the centrelines of the actual struc-

tures. With a 0.2 m concrete core and 10 mm steel plates, the distance between the centrelines is 0.105 m.

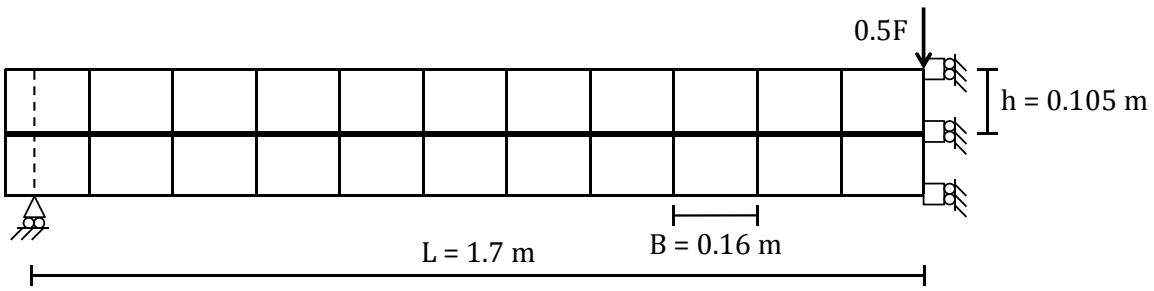

Figure 21. The element configuration in the element model.

Thin horizontal lines in fig. 21 represent the steel plates. Vertical solid lines represent the connection between steel and concrete. Thick horizontal lines represent the concrete core. Dashed vertical lines connect the concrete core to the support.

The stiffness values of the elements are calculated from the geometrical properties of the structure. The second moment of inertia can be evaluated with the well-known equation:

$$I = \frac{dh^3}{12}, \tag{4}$$

where h is h_c for the concrete core and t_s for the steel plates, and d is the depth of the structure. The cross-sectional area for the elements, A, is calculated using the same dimensions as the bending stiffness:

$$A = dh. \tag{5}$$

The dashed vertical elements in fig. 42 are given a high compressive stiffness to guide the reaction force from the support to the concrete core and a negligible bending stiffness, so that they do not affect the slipping phenomenon. The solid vertical elements represent the connection between the studded steel plates and the concrete. They have high compression stiffness and a bending stiffness that is defined to match a shear spring constant calculated in the stud module.

Shear springs between the concrete and steel plates are approximated with beam elements that connect the centre of the concrete to the centre of the steel plates. They have an identical force-displacement response as the spring would have. The relationship between the deflection and a loading force for a spring is

$$v = \frac{F}{n_s k}, \tag{6}$$

where v is the deflection, F the shear force, $n_{springs}$ the number of springs in parallel and k is the spring constant.

The vertical beams in the model are given a stiffness that matches the spring constant calculated in the stud module. Figure 22 shows the beam whose left end represents concrete core of an SC-structure. The right end represents the connection of the stud to the steel plates.

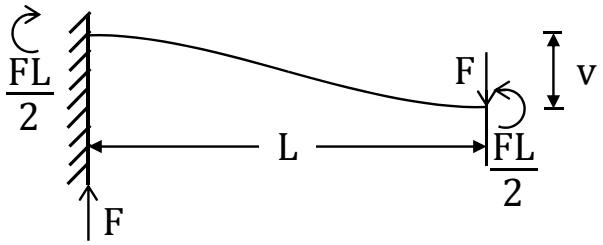

Figure 22. The relation between force and deflection in a beam, which is fixed at one end and free to move, but not rotate, at the other.

The deflection v for a beam with the border conditions and load depicted in the above figure is given by

$$v = \frac{FL^3}{12EI'} \tag{7}$$

where L is the length of the beam, E is the modulus of elasticity and I is the second moment of inertia. By equating equations 6 and 7, a relationship between the spring constant and the required beam stiffness is established as

$$\frac{F}{n_s k} = \frac{FL^3}{12EI'} \tag{8}$$

from which the stiffness of the beam can now be solved as

$$EI = \frac{n_s k L^3}{12}. \tag{9}$$

This stiffness, EI, is used in the element model for the vertical beams representing the stud's connection between the steel plates and the concrete core.

Figure 23 shows an overview of the models and modules used to calculate the effects of three point bending experiment of an SC-structure.

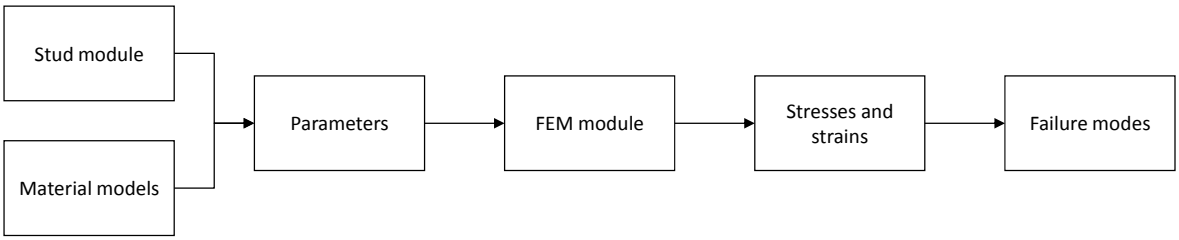

Figure 23. The relationship between the modules for calculating an SC-structure in bending.

6.3 Case-specific modules

This case utilizes the FEM module and the stud module for calculating an input parameter.

6.3.1 The FEM module

The finite element method is a numerical approximation method for solving differential equations with given boundary conditions. This applies especially well for structural mechanics.

This module utilises beam elements with six degrees of freedom. The elements are considered to have uniform stiffness from end to end. Even though the finite element method is an approximate method, the beam equations are solved exactly, if the loads are modelled to be on the node points.

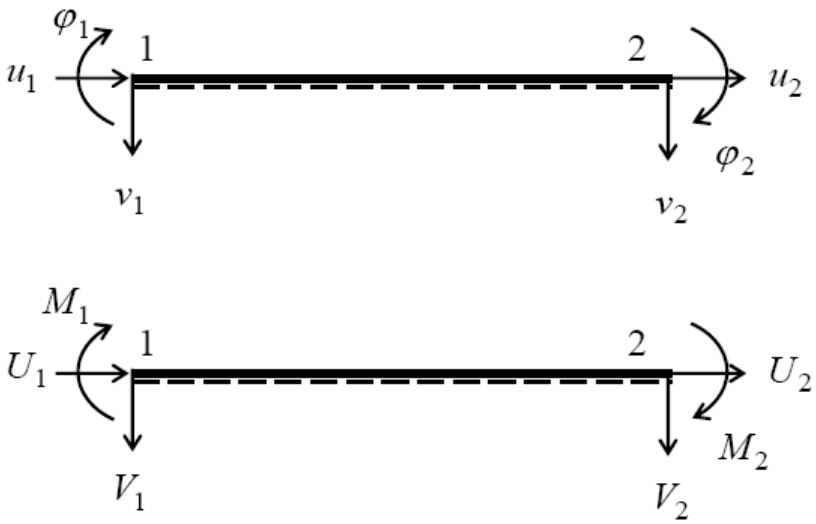

Figure 24. The loads and their corresponding deflections for an element. (Agarwal, 2014)

Using the nomenclature in fig. 24, the local displacements and loads can be written in vector-form as follows:

$$f = \begin{pmatrix} U_1 \\ V_1 \\ M_1 \\ U_2 \\ V_2 \\ M_2 \end{pmatrix}, u = \begin{pmatrix} u_1 \\ v_1 \\ \varphi_1 \\ u_2 \\ v_2 \\ \varphi_2 \end{pmatrix} \quad (10),\ (11)$$

The known relationships between f and u in an element's local coordinates can be gathered into a stiffness matrix K_e:

$$K_e = \begin{bmatrix} \frac{\mathrm{AE}}{\mathrm{L}} & 0 & 0 & -\frac{\mathrm{AE}}{\mathrm{L}} & 0 & 0 \\ 0 & 12\frac{\mathrm{EI}}{\mathrm{L}^3} & 6\frac{\mathrm{EI}}{\mathrm{L}^2} & 0 & -12\frac{\mathrm{EI}}{\mathrm{L}^3} & 6\frac{\mathrm{EI}}{\mathrm{L}^2} \\ 0 & 6\frac{\mathrm{EI}}{\mathrm{L}^2} & 4\frac{\mathrm{EI}}{\mathrm{L}} & 0 & -6\frac{\mathrm{EI}}{\mathrm{L}^2} & 2\frac{\mathrm{EI}}{\mathrm{L}} \\ -\frac{\mathrm{AE}}{\mathrm{L}} & 0 & 0 & \frac{\mathrm{AE}}{\mathrm{L}} & 0 & 0 \\ 0 & -12\frac{\mathrm{EI}}{\mathrm{L}^3} & -6\frac{\mathrm{EI}}{\mathrm{L}^2} & 0 & 12\frac{\mathrm{EI}}{\mathrm{L}^3} & -6\frac{\mathrm{EI}}{\mathrm{L}^2} \\ 0 & 6\frac{\mathrm{EI}}{\mathrm{L}^2} & 2\frac{\mathrm{EI}}{\mathrm{L}} & 0 & -6\frac{\mathrm{EI}}{\mathrm{L}^2} & 4\frac{\mathrm{EI}}{\mathrm{L}} \end{bmatrix} \quad (12)$$

To account for elements in different orientations relative to each other, their stiffness matrix must be transformed. Transforming the stiffness matrices of elements in local or element specific coordinates to global coordinates is done with the following equation:

$$\left[K_{eg}\right] = [T]^T [K_e][T] \quad (13)$$

where transformation matrix T is defined as follows:

$$T = \begin{bmatrix} \cos(\theta) & \sin(\theta) & 0 & 0 & 0 & 0 \\ -\sin(\theta) & \cos(\theta) & 0 & 0 & 0 & 0 \\ 0 & 0 & 1 & 0 & 0 & 0 \\ 0 & 0 & 0 & \cos(\theta) & \sin(\theta) & 0 \\ 0 & 0 & 0 & -\sin(\theta) & \cos(\theta) & 0 \\ 0 & 0 & 0 & 0 & 0 & 1 \end{bmatrix} \quad (14)$$

where θ is the angle between the coordinate system of the element and a globally defined baseline. The element stiffness matrices K_{eg} are gathered together into a global stiffness matrix K in such a way that the relationship

$$\{f\} = [K]\{u\}, \tag{15}$$

where f is vector containing all the external loads and u a vector containing all the displacements, holds true. Any node can be constrained against any combination of displacements by adding a spring constant to entries on the diagonal corresponding to desired direction and type of displacement to be constricted. Fixed nodes are represented by an infinite spring constant. Finally solving for the displacements yields:

$$\{u\} = [K]^{-1}\{f\} \tag{16}$$

The above procedure solves linear problems, but this model is improved by accounting for the cracking of the concrete core in tension, yielding of the steel plate in tension and using a non-linear shear-slip response in the studs. The solution used here for the non-linear material parameters is the secant module method. Cracking is modelled by modifying the geometric properties of the elements through their nodes' coordinates.

6.3.2 Secant module method for the shear springs

Non-linearity in the elements representing the studs is implemented by recalculating the value of the stiffness of the beam given in eq. (9) for the next iteration, using the secant modulus of the shear spring calculated with the stress state resulting from the previous iteration. Each stud element is updated based on its own stress state. During testing, this was usually found to converge quickly, but the yielding of the steel plates requires additional controls to reduce the number of iterations needed for the solution to converge.

The studs' shear force-slip relationship is based on test results conducted on studs used in the liner at the OL3 NPP. These test results are also used as a benchmark for the stud module and can be seen in fig. 32. The initial response between the shear force and slip is linear, up until half of the ultimate shear strength of the stud Q_u is reached at a slip of ε_0. The slope of the first linear portion of the curve is calculated with the stud module. At a slip of ε_0 + 1 mm, the shear force reaches 75 % of Q_u and at 4 mm it is considered to reach 100 % of Q_u. The value of slip corresponding to the first turn in the curve is

$$\varepsilon_0 = \frac{0{,}5\mathrm{Q_u}}{\mathrm{k}}, \tag{17}$$

where $\mathrm{Q_u}$ is the ultimate strength of the stud and k the spring constant calculated in the stud module. Figure 25 shows the previously defined shear-slip curve in blue and the studs' secant modulus of stiffness in green. The secant modulus is evaluated with the following simple relationship:

$$k_{sec} = \frac{Q}{\varepsilon}, \tag{18}$$

where Q is the shear force and ε is the slip. The value of k_{sec} is used in the next iteration of the FEM evaluation for the stud in question. This iteration converges quickly, because the change in the secant modulus results in a much smaller change after the iteration. In the yielding of the steel plate, however, the same procedure results in an almost equal change after the iteration.

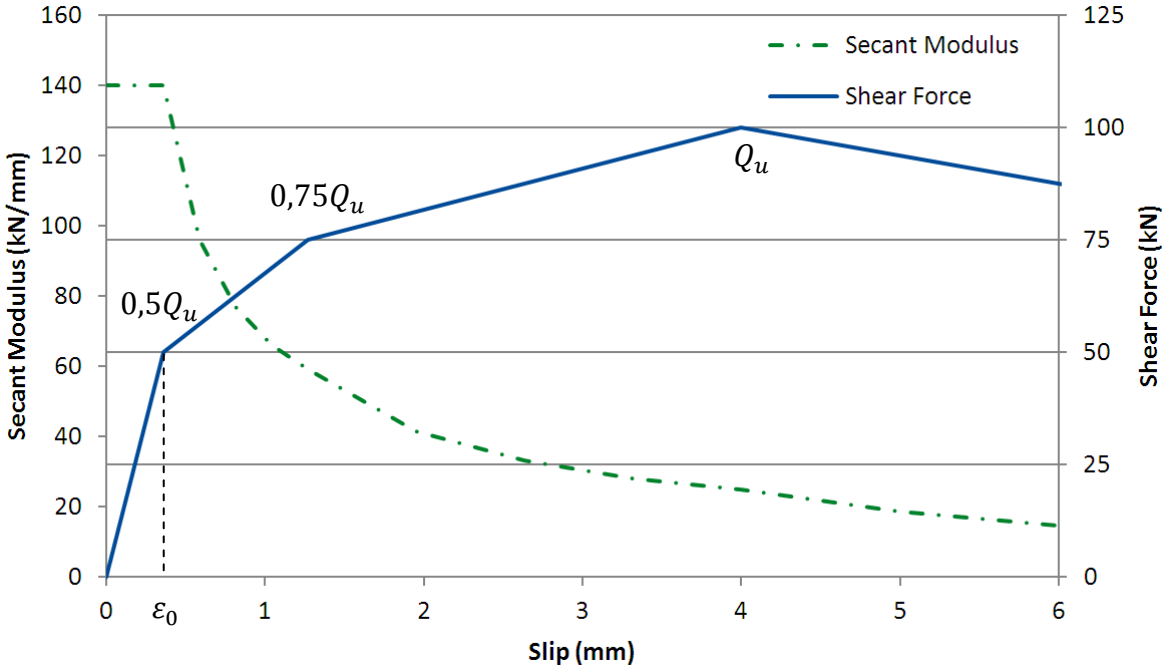

Figure 25. Shear modulus and secant modulus for the stiffness of the shear springs as a function of slip for a 25 mm stud.

6.3.3 Yielding of the steel plates

The material in the steel plates is modelled with the constitutive relationship shown in figure 26. The yielding strength of steel was set to 462 MPa and the ultimate strength to 520 MPa to match the values used in the loading experiment used as a benchmark. The first part of the slope is defined by the MOE of steel, which was set as 207 GPa.

To help the secant module method in the elements that are yielding converge faster, an algorithm based on the bisection method was created. It is described in appendix 1.

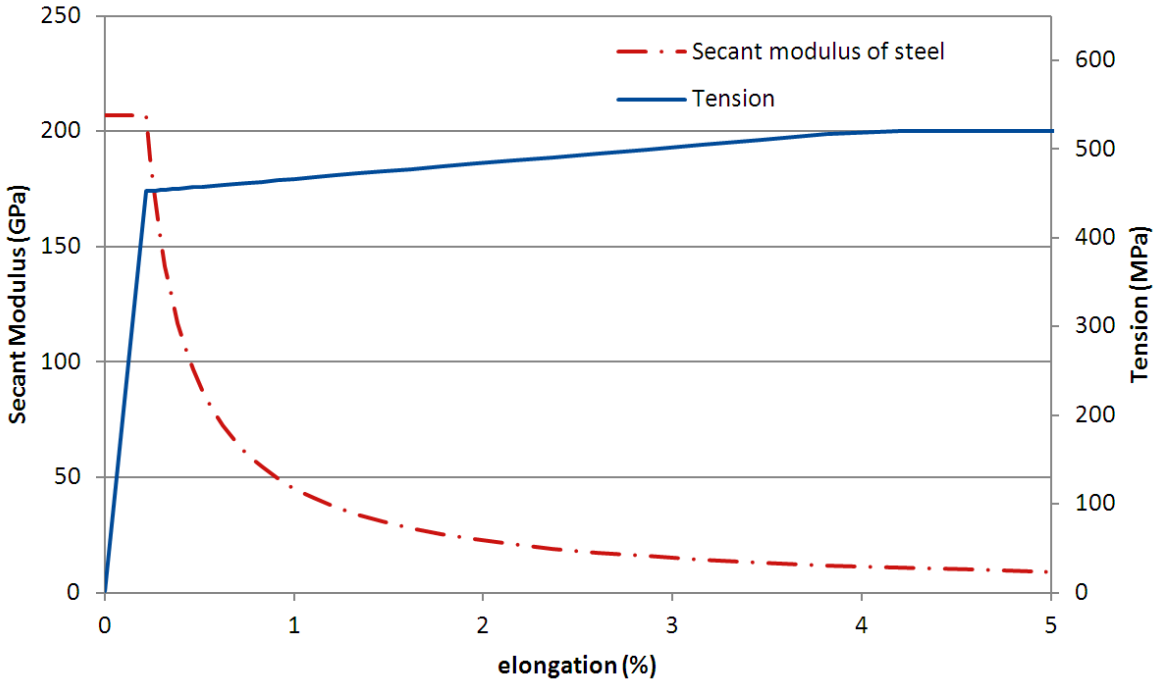

Figure 26. The material model used for the steel plates. The secant module and tension are graphed in different scales as a function of elongation.

6.3.4 Concrete cracking

The effects of concrete cracking are modelled by reducing the thickness of the concrete beam elements in response to the curvature of the cross-section. The concrete beam elements are also moved to the compression side of the structure accordingly, so that the internal forces of the cross-section are balanced correctly. This procedure strives to represent the fact that concrete has hardly any strength in tension.

The neutral axis is calculated linearly from the displacements in the steel plates in the area with the highest curvature i.e. the middle of the structure. The concrete is considered to have a little strength in tension, which is accounted for in the height of the effective concrete beam elements. The allowed strain in the concrete is

$$\varepsilon_{ct,max} = \frac{f_{ctm}}{E_c}, \tag{19}$$

where f_{ctm} is the strength of concrete in tension according to the Eurocodes (SFS, 2005 p. 29) and E_c is modulus of elasticity of concrete.

The effective thickness is modelled uniformly along the whole length of the beam as shown in fig. 27. This is done, because calculating the amount of cracking for each element separately resulted in a non-convergent iteration process. In that

case, the areas of high and low effective thickness wandered along the length of the structure during the iteration process.

Figure 27. Top image: the element net is superimposed on the cross-section of a 220 mm thick SC-wall with 10 mm steel plates. The bottom image shows how the effective thickness $h_{c,eff}$ of the concrete under a bending moment is accounted for in the FEM model.

6.3.5 Verifying the cross-section procedure

During the creation and testing phase of the element model, a simple cross-section model was used to check the strain state of the different parts of the SC-structure. The cross-section model is completely independent from the element model. It works by creating a strain state across the cross-section using only two parameters, which are the location of the neutral axis and the curvature of the beam. The cross-section of the structure is assumed to remain planar, with no slip between the steel plates and the concrete.

The location of the neutral axis and the curvature are solved for a given bending moment by using the “Solver” tool in Excel. The tool searches for the values of the two variables that satisfy the border conditions, which are the equilibrium of the internal forces caused by the strains of the parts and the equilibrium of the given moment and the moment caused by the strain state of the parts. The horizontal axis in fig. 28 represents a horizontal slice of a structure oriented as in fig. 19.

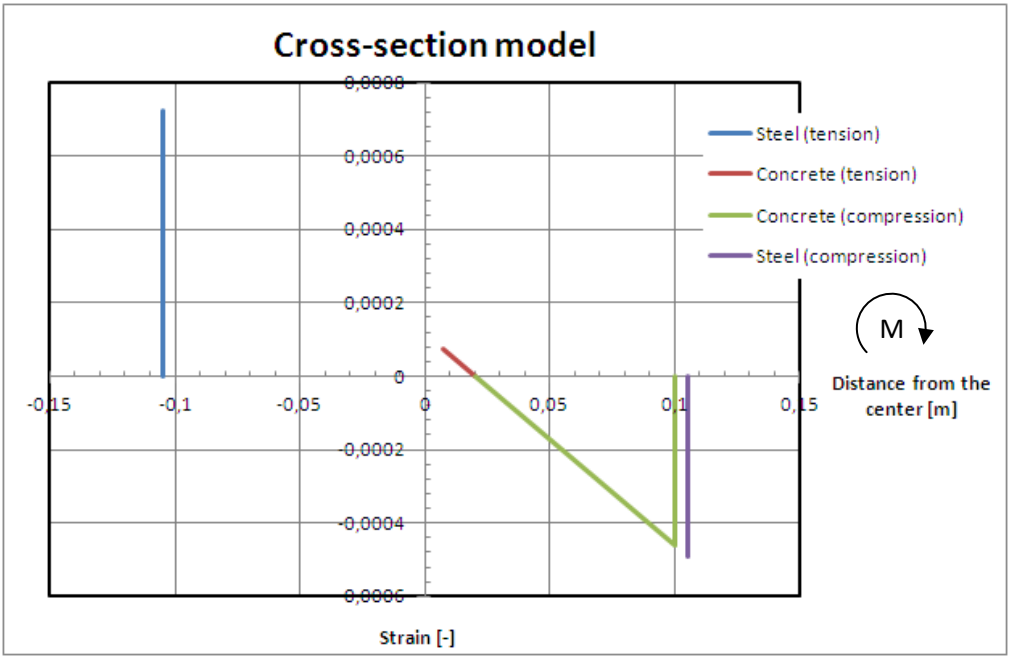

Figure 28. An example of the output from the cross-section model. The structure under a bending load has 10 mm steel plates on both sides and a 200 mm concrete core. What is shown is strain state caused by a 300 kNm bending moment.

To make the results comparable to the element model, the studs in the element model were given a near-infinite shear spring constant, which keeps the cross-section planar. In this case the models returned identical results, as expected.

6.3.6 The stud module

The purpose of the stud module is to determine the force-to-slip ratio or spring constant of a single stud, which can be used in the truss model to account for slippage. The modelling analogy is of a beam on an elastic surface, which has a unit force applied to the end of it as shown in figure 29. The beam is considered to be supported by vertical springs. The deflection of the end is considered as the slip. The spring constant k can be calculated with the following equation

$$k = \frac{\mathrm{F}}{\mathrm{w}} \tag{20}$$

where F is the force affecting the end of the beam and w is the deflection at the end of the beam.

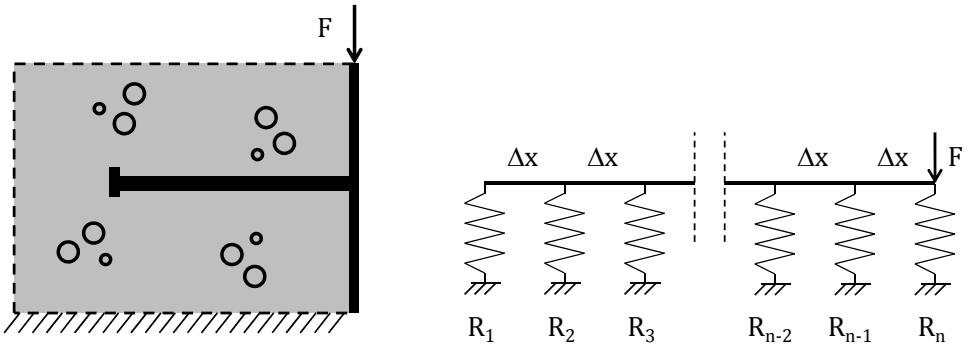

Figure 29. The figure on the left represents the real world structure and the picture on the right shows how a stud is modelled as a beam on an elastic surface. To avoid confusion, it should be noted that the orientation of the pictured structure is different from the element model.

The model consists of n beam elements in a straight line. Each element is supported at each end by springs, which represent the concrete around the stud. The reaction forces R_j of the springs are calculated with equations 21, 22 and 23. Equations 22 and 23 represent the springs at the ends of the stud.

$$R_j = \frac{\Delta x \cdot d \cdot c}{8}\left(w_{j-1} + 6w_j + w_{j+1}\right), j = [2 \dots n-1] \tag{21}$$

$$R_1 = \frac{\Delta x \cdot d \cdot c}{8}(3w_1 + w_2) \tag{22}$$

$$R_n = \frac{\Delta x \cdot d \cdot c}{8}(w_{n-1} + 3w_n) \tag{23}$$

In the equations above Δx is the length of the beam element, d the diameter of the stud, c the coefficient of subgrade reaction and w_j the deflection at spring j. The length of an element is obtainable as follows:

$$\Delta x = \frac{L_{stud}}{n_s - 1} \tag{24}$$

The subgrade reaction distribution is considered linear along an element. There is considerable uncertainty in the modulus of subgrade reaction, but an approximation can be calculated from equation 25.

$$c = \frac{E_c}{0.024\ \mathrm{m}} \tag{25}$$

where E_c is the modulus of elasticity for concrete. This value gives results in line with empirical test results (Test report NEEA-G/2007/en/1024 appendix B p. insert 5) and previous studies (Leskelä, 1986).

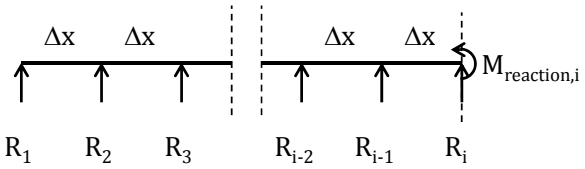

Figure 30. Internal moments in the stud on an elastic surface.

The equilibrium of forces on the left side of any point at a spring, denoted by i, caused by reaction forces in the springs and external forces, which are zero, except at the right end, yields the following equation using the nomenclature in fig. 30:

$$M_{reaction,i} = \sum_{j=1}^{i} R_j(i-j)\Delta x. \tag{26}$$

Bending of the beam causes the following moment at spring i:

$$M_{bending,i} = -\frac{E_s I_{stud}}{\Delta x^2}(w_{i-1} - 2w_i + w_{i+1}), i = [2 \dots n-1] \tag{27}$$

where E_s is the modulus of elasticity of steel and I_{stud} the second moment of inertia of the stud, which is calculated as follows:

$$I_{stud} = \frac{\pi r^4}{4} \tag{28}$$

where r is the radius of the stud. The moments must cancel each other out in a static structure, which leads to the following condition:

$$M_{bending,i} + M_{reaction,i} = 0 \tag{29}$$

This leads to n-2 equations with n unknown deflections w_i. The final two necessary equations are obtained from the balance of external forces conditions.

$$\sum_{i=1}^{n} R_i = F \tag{30}$$

$$\sum_{i=1}^{n} R_i(n - \mathrm{i})\Delta x = M_n = 0 \tag{31}$$

The equations can now be written in matrix form:

$$[K]\{w\} = \{f\} \tag{32}$$

where K is an n by n stiffness matrix and w the deflection vector of length n and f is the load vector of length n. The deflections w_i can be solved as follows:

$$\{w\} = [K]^{-1}\{f\} \tag{33}$$

Figure 31 shows a graphical representation of the deflection of a stud loaded by a unit force in the downward direction at the right end of it. Inserting the deflection at the end of the stud into equation 20 yields a spring constant, k, of $5.48 \cdot 10^7 \frac{\mathrm{N}}{\mathrm{m}}$ for an 8 mm thick stud.

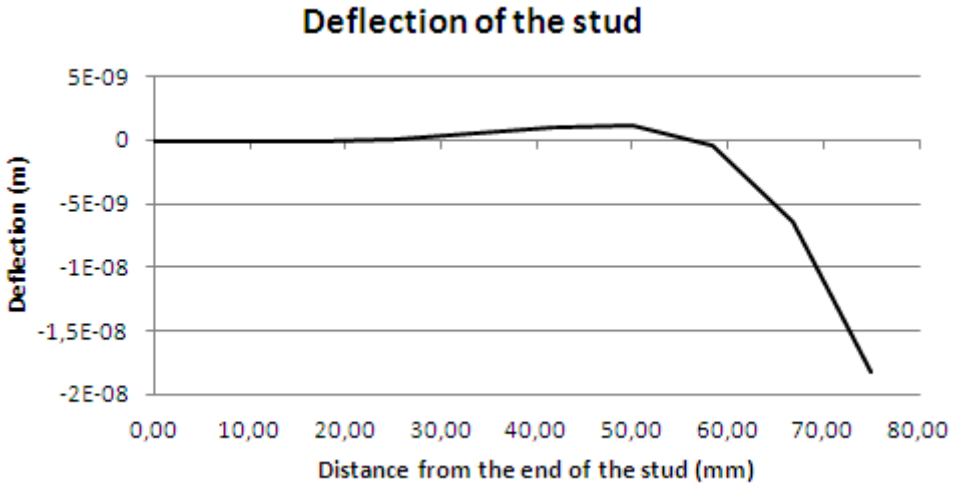

Figure 31. The calculated deflection of an 8 mm by 75 mm stud caused by a unit force.

6.3.7 Verifying the stud model

Shear studs used in the liner of the containment building in Olkiluoto 3 nuclear power plant were tested to ensure adequate ductility in cases of extreme deformations. The load displacement curve was the desired result for the test.

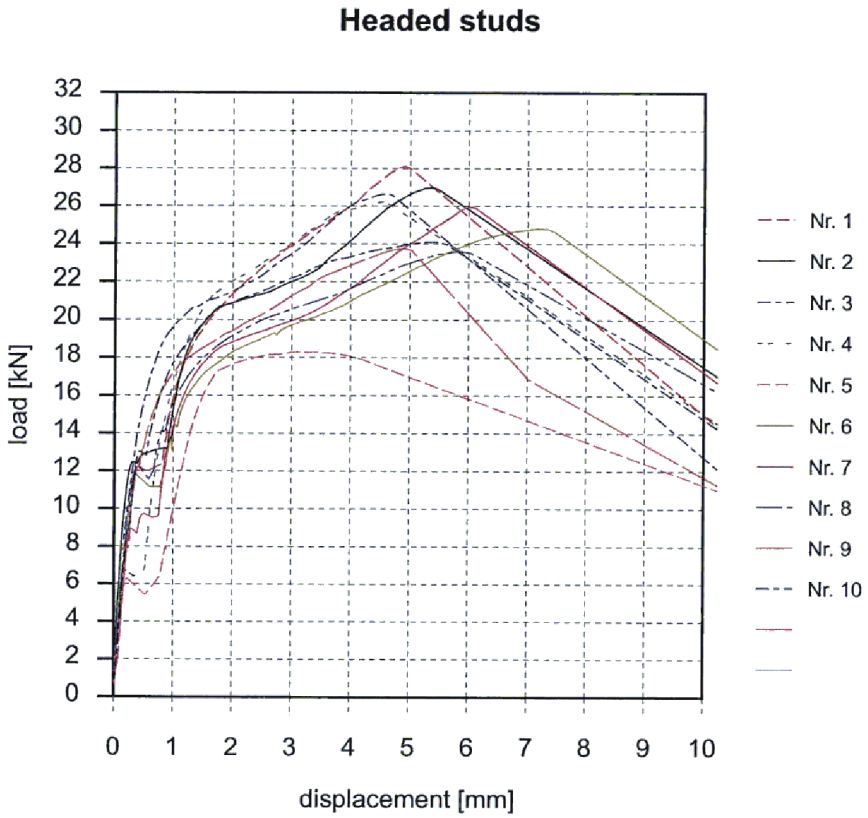

Figure 32. A shear-displacement graph of 8 mm by 75 mm Nelson-bolt studs. (Jeschke & Ostermann, 2008 Appendix B p. “Insert 5”)

The slope of the linear part of the curve was measured for each stud. The graphs were available for each stud individually. (Jeschke & Ostermann, 2008 Appendix B pp. “Insert 6”-“Insert 15 and “Insert 18”-“Insert 27”) The results are in tables 1 and 2.

Table 1. Spring constants calculated from the abovementioned experimental results.

Test no.	Force [N]	Deflection [mm]	k [N/m]	Measured / Calculated
1	7000	0,17	4,12E+07	0,75
2	9000	0,2	4,50E+07	0,82
3	10000	0,2	5,00E+07	0,91
4	7000	0,09	7,78E+07	1,42
5	9000	0,1	9,00E+07	1,64
6	7000	0,07	1,00E+08	1,82
7	8000	0,1	8,00E+07	1,46
8	9000	0,13	6,92E+07	1,26
9	6000	0,24	2,50E+07	0,46
10	12000	0,15	8,00E+07	1,46
			Average	1,20

Table 2. More spring constants calculated from abovementioned experimental results.

Test no.	Force [N]	Deflection [mm]	k [N/m]	Measured / Calculated
1	7000	0,1	7,00E+07	1,28
2	11000	0,2	5,50E+07	1,00
3	4000	0,05	8,00E+07	1,46
4	6000	0,1	6,00E+07	1,09
5	5000	0,16	3,13E+07	0,57
6	8000	0,13	6,15E+07	1,12
7	8000	0,2	4,00E+07	0,73
8	11000	0,35	3,14E+07	0,57
9	12000	0,36	3,33E+07	0,61
10	8000	0,2	4,00E+07	0,73
			Average	0,92

Tables 1 and 2 list the measured spring constants, which are compared to the value calculated by the stud module for a stud of similar dimensions. On average the calculated value is a little below the measured value.

The JEAC standard gives the following guidance for determining the maximum diameter of the studs for a corresponding thickness of the steel plate in the table below.

Table 3. Maximum diameter of a stud for different steel plate thicknesses. (JEA, 2010 p. 2.2-10)

Thickness of steel plate t_s	**Maximum diameter d_{max}**
3.2 mm	9 mm
4,5 mm	13 mm
6 mm	16 mm
9 mm	22 mm
12 mm	25 mm

The European technical approval (ETA) for Nelson bolts provides conservative values for the shear-slip relationship. The resulting spring constant is lower than the value calculated with the stud module. However, when comparing it to the shear slip curve at a slip value of 1.5 mm shown in fig. 25, the match is much better.

Table 4. The shear force corresponding to a 1.5 mm slip according to the European Technical Approval report for Nelson-headed studs. The diameter and Shear force are given in the report and the spring constant is calculated from these values. (DIBT, 2003, annex 6)

Diameter	Shear force	Spring constant
10 mm	15 kN	10.0 MN/m
13 mm	20 kN	13.3 MN/m
16 mm	30 kN	20.0 MN/m
19 mm	45 kN	30.0 MN/m
22 mm	60 kN	40.0 MN/m
25 mm	75 kN	50.0 MN/m

6.4 Verifying the element model

The model was verified by comparing it against experimental results. A study by McKinley et al. (2002) compared the shear studs of a traditional double skin composite structure to bi-steel shear studs, which are welded to both of the steel plates. The loading experiments performed on the traditional shear studs will be used as comparison data to verify the truss model.

6.4.1 Loading experiment

Geometric and material properties available from the experiment are in table 5. The T/t-ratio of the SC-structure is 22, which is below the applicability of the JEAC standard. The thickness of the studs was not mentioned, but judging from close up pictures of the test setup, a diameter of at least 25 mm was used.

Table 5. Properties of the beams in the loading experiment

Table 1
Test panel dimensions

Panel name	Series	Construction	Span L (mm)	Width b (mm)	Plate depth t (mm)	Bar spacing/plate depth ratio s/t	Concrete depth h_c (mm)	Steel strength f_y (N mm^{-2})	Concrete strength f_{cu} (N mm^{-2})
Stud2	1	Stud	3400	1000	10	16	200	452.2	55.0
Stud2b	1	Stud	3400	1000	10	16	200	452.2	56.0
City1	1	Bi-Steel	3400	1000	10	20	200	452.2	53.3
City2	1	Bi-Steel	3400	1000	10	20	200	452.2	58.0

Other material parameters used are the MOE of concrete, which was chosen to be 27 GPa, the MOE of steel, and the ultimate strength of steel, which are available in fig. 26. The load-deflection curve produced using the previously mentioned parameters is shown in fig. 33.

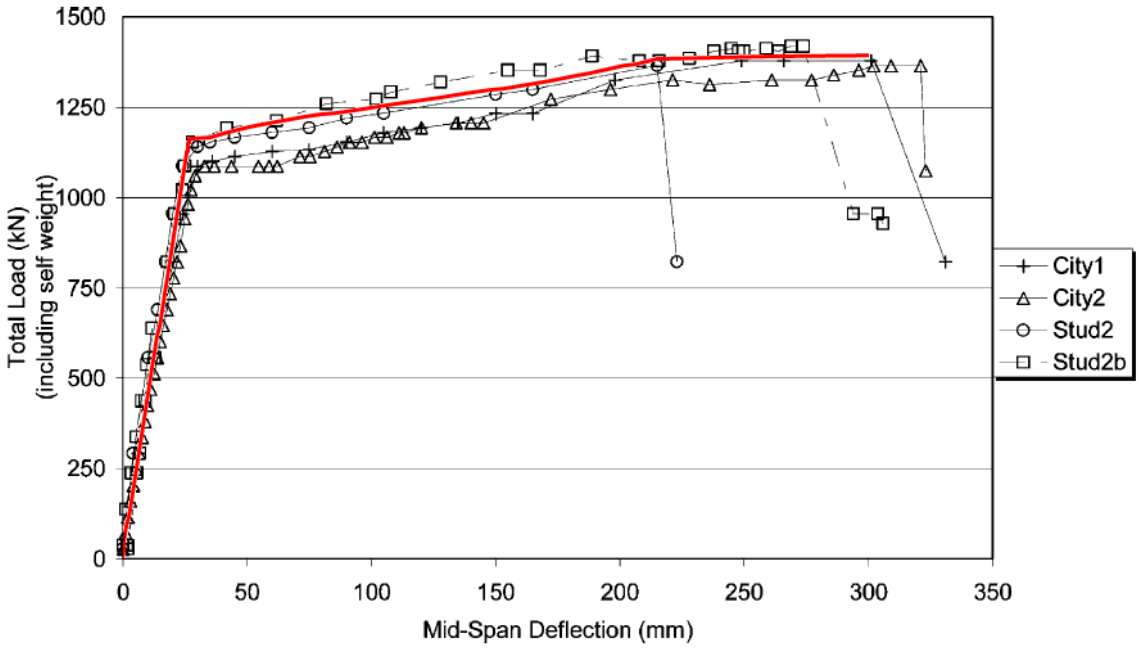

Figure 33. Comparison of the load-deflection results from the experiment by McKinley et al. (2002) and the element model.

In the figure above, the red line represents the load-deflection curve calculated using the element model. It is superimposed on the experimental results measured by McKinley et al. (2002). Stud2 and Stud2b are used as a benchmark. The scales of the axes in the superimposed curve are within one pixel of the scales of the source image. There is a change in slope at load of around 100 kN, which is caused by cracking.

The calculated load-deflection curve matches the experimental one well. Only ε_u was fitted to get the correct slope after the yield point. The interpreted failure mechanism was concrete crushing caused by yielding of the steel plate under tension. McKinley et al. (2002) mention that the properties of steel after yielding are difficult to predict without tests, which makes modelling without experimental data difficult and unreliable. The following analysis will concentrate on the yield point and its effects on the reliability of the structure.

6.5 Analysis of three different T/t-ratios

The element model is run iteratively with an increasing load, until the solution failed to converge. Three different groups of input parameters are used to represent structures with T/t-ratios of 30, 52 and 152. They are shown in table 6. The other parameters are the same as in the verification calculations.

Table 6. The geometric parameters used in the simulations to achieve the desired T/t-ratios.

T/t-ratio	Concrete thickness	Steel plate thickness	Diameter of the stud
30,5	200 mm	7 mm	16 mm
52	300 mm	6 mm	16 mm
152	900 mm	6 mm	16 mm

A minimum steel plate thickness of 6 mm was chosen to comply with the JEAC standards requirements (JEA, 2008 p. 2.2-11) regarding the B/t-ratio, in which B is the distance between the studs. The equation used to determine B is

$$\frac{B}{t} \leq \frac{600}{\sqrt{F_{cs}}}, \tag{34}$$

where F_{cs} is the buckling-limited allowable compression in the steel plate. It is calculated as follows:

$$F_{cs} \leq \frac{\zeta_d E_s \pi^2}{12 k_b^2 \left(\frac{B}{t}\right)^2}, \tag{35}$$

where ζ_d is a reduction (1.0 for short-term and 2/3 for long-term loading), E_s is the MOE of the steel plates, k_b is the buckling coefficient, which is 0.7 for a plate supported by studs (JEA, 2008 p. 2.2-14).

6.6 Results

The results were calculated by using the Monte Carlo module to control the repetitive input of the increasing load and saving the result for each iteration as well as other parameters, such as the tolerance value describing the convergence of the secant module procedure. After the simulation, which was usually left over-night to complete, the failure load was identified by scanning through the results until a tolerance value was found that indicated that the secant module procedure for the studs stiffness calculations had not converged. The results are shown in figure 34. The lower the, T/t-ratio, the more the structure deflects under the load before failure.

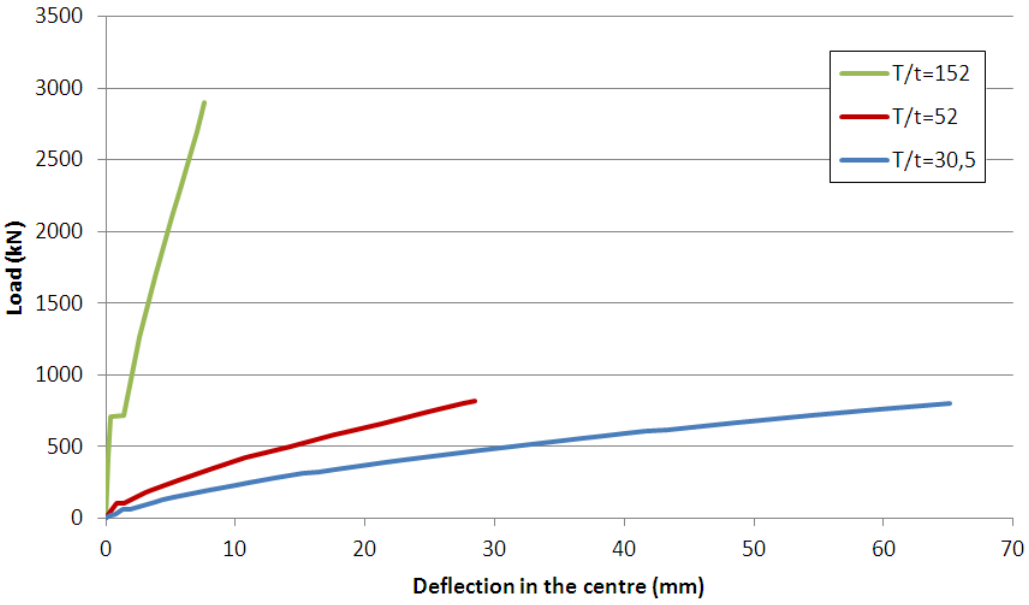

Figure 34. The results of the loading calculation. The first change in each slope is caused by cracking of the concrete. The ends of the curves represent the load at which failure occurred.

The weaker studs used in these simulations, compared to the studs in the benchmark, caused a different failure mechanism to occur. The failure was caused by the studs slipping so far that the secant modulus began to decline as the slip increased i.e. past the point of the ultimate shear strength shown in fig. 25, which caused the solution to diverge. The differences in T/t-ratio, which for the benchmark structure was below the minimum applicability of the JEAC standard for SC-structures, and the significantly smaller studs used in the simulation, seem to cause a change in the failure mechanism.

When using a high enough stud density and studs of high strength, as in the benchmark structure, the strains can be assumed to be linearly distributed in the cross-section without significant error. However, the structures using smaller studs seem to be affected more by the sliding phenomenon. According to fig. 35 from JEAC, taking slipping at the studs into account, the curvature of the structure is increased by roughly 15 % compared to an assumption of cross-sectional planarity in bending.

The structure with a T/t-ratio of 152 fails at a curvature of about 0.0076 rad/m calculated from the concrete beam elements at the middle of the structure. This is quite close the curvature corresponding to failure in fig. 35, which shows the results of a bending experiment of a smaller SC-structure with a similar T/t-ratio.

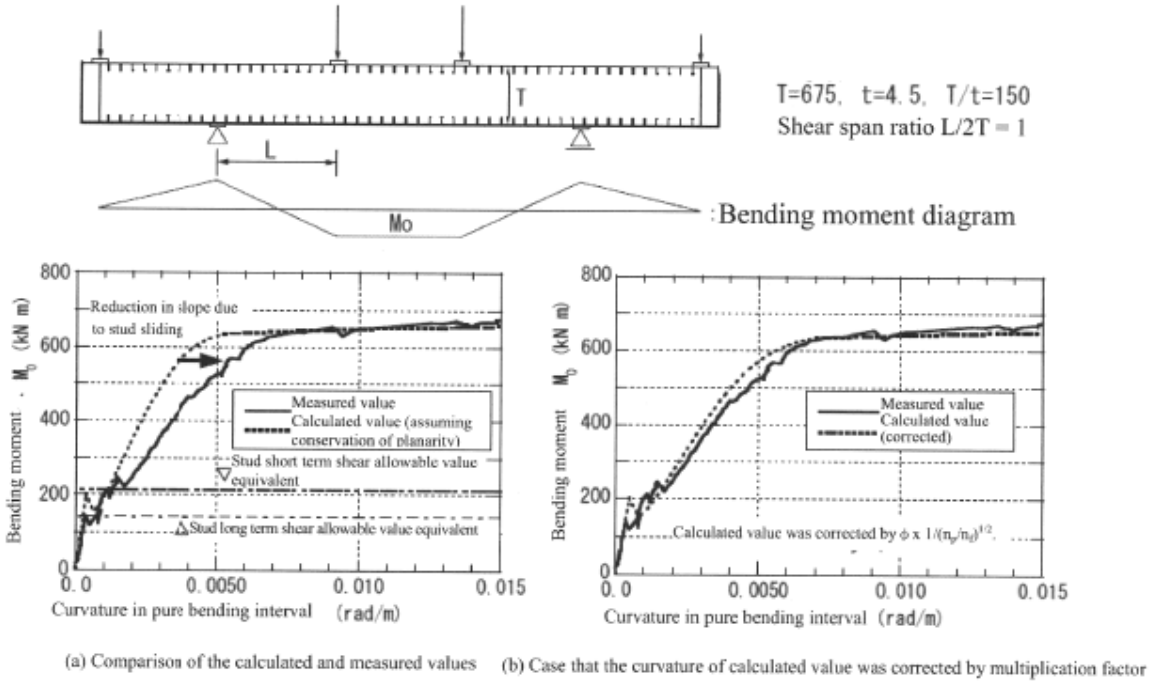

Explanatory Figure 2.2.2-1 Comparison between the measured results and the calculated results assuming conservation of planarity

Figure 35. Results of a four point bending experiment shown in the JEAC standard as reference material. (JEA, 2008 p. 2.2-26)

In conclusion, a model was created that fits the experimental test results used as a benchmark with reasonable accuracy. It can uncover multiple failure conditions and the element model gives large amounts of data for further analysis. Any cell in the spreadsheet containing the element model can be chosen to be scrutinised, while changing any input parameter. However, the computer code controlling the non-linear portion of the calculation procedure needs optimization to make creating large amounts of data for statistical analysis a more viable option.

If some of the NPPs being proposed at the moment end up using SC-structures, their bending properties can be modelled and studied in detail. In that case, an interesting study would be to find out what combination of T/t-ratio and stud size borders the two different failure mechanisms. The effects of shearing forces in the direction of the wall should also be studied, since they are more important in seismic fragility studies.

7 Case 2: Prestressed tendons

Concrete has highly varying material properties depending on the type of strain it is under. In tension, cracks open up, which lead to problems with leak-tightness and accelerated aging related degradation. In the case of NPP containment buildings, the critical design scenario is a LOCA, which causes internal pressure loads that cause tension in the concrete structures. Prestressing forces must cancel out this tension. The specific prestressing type to be modelled is a multistrand post-tensioning system actively anchored at both ends.

The goal of this study is to find out what the most important factors affecting prestressing losses are. Of specific interest is the effect of a vertical deviation of the path of the tendon from the cross-section plane, which occurs in the vicinity of an opening in the shell. Statistical data on the construction materials is available from sample tests conducted at the construction site. Concrete properties including strength, modulus of elasticity and creep factors have been measured. The relaxation of the tendon has also been tested. Calculations performed in the design of the tendons in the OL3 project are used to verify the calculation model.

7.1 The calculation model

Prestressing losses can be divided into instantaneous and long-term losses. Instantaneous losses are realised when the tendons are tensioned. This includes strains caused by Poisson's effect from vertical tendons that are tensioned after the horizontal tendon being examined. Long-term losses happen because of creep and shrinkage of the concrete and relaxation in the steel in tension. The instantaneous losses included in the calculations are due to friction, elastic shortening of the concrete and anchor slipping. The included long-term losses for concrete are autogenous and drying shrinkage and basic and drying creep. The equations used to calculate the pre-tensioning losses are presented in the next sub chapters.

The geometric paths of the all the tendons in an example containment building are illustrated in fig. 36. The OL3 containment building being modelled is fundamentally very similar. Calculations will concentrate on the tendons with the largest vertical deviations, whose paths run closest to the material hatch similar to the one pictured in fig. 36.

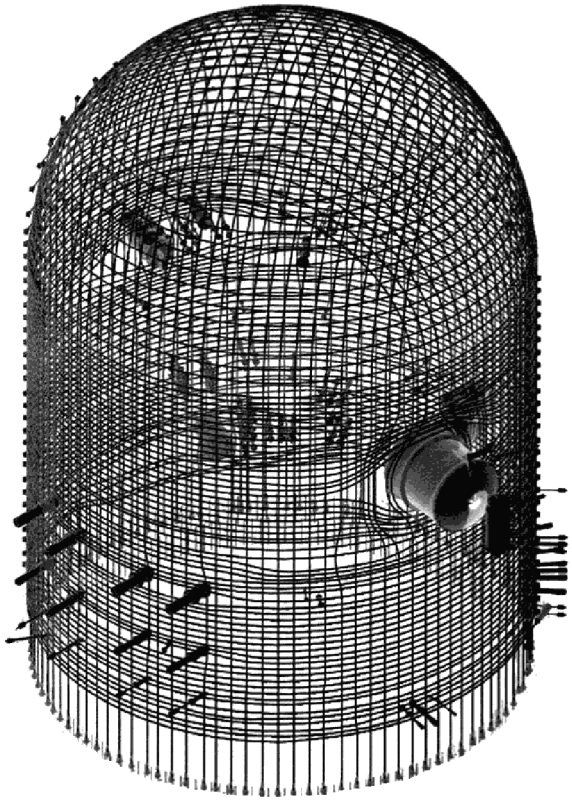

Figure 36. Paths of tendons in a containment building. To the right of the middle of the picture there is an opening known as the material hatch, around which the tendons must be routed. (Varpasuo, 2002, fig. 5)

Both ends of the tendons are anchored at the same buttress, which means the tendons reach around the whole structure, which leads to significant friction losses in the prestressing tension. Figure 37 shows an aerial view of the path of a tendon. The tendon may also deviate from the plane horizontal plane of the cross-section of a cylinder, as shown in fig. 38. The shape of the vertical deviation is created by fitting a parabolic function to the starting point of the deviation and the point of maximum deviation, which are available in the design plans of the OL3 NPP.

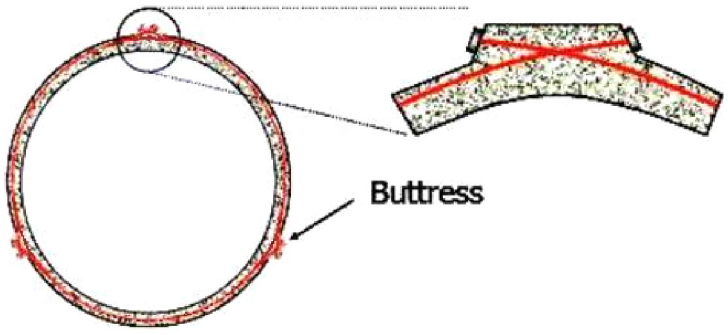

Figure 37. A top view of the containment-building cross-section showing the configuration of the tendons and the buttresses. The close-up view on the right shows both ends of the same tendon. (Mishra, 201?)

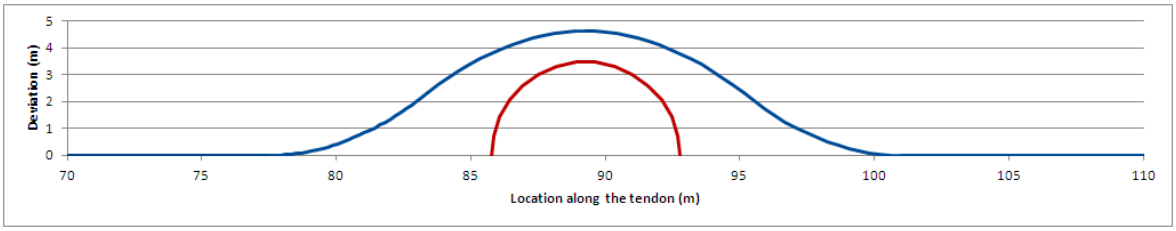

Figure 38. The vertical deviation of the tendon (in blue) and an obstacle e.g. an equipment hatch centred at 89.65 m (in red). The distance needed for the deviation to reach the apex from base level is 11.75 m, creating an area of effect of 23.5 m.

Figure 39 shows a cross-section of the containment building wall with the steel liner on the left and horizontal tendons on the right. Passive reinforcement bars are also included. The dashed line represents the share of the area of concrete being affected by a group of three tendons. The three tendons are grouped together, because they have slightly different tension profiles along their length relative to each other. The differences are caused by the relative location of the obstacle and higher friction associated with it. The tension profiles of the tendons can be seen in fig. 40.

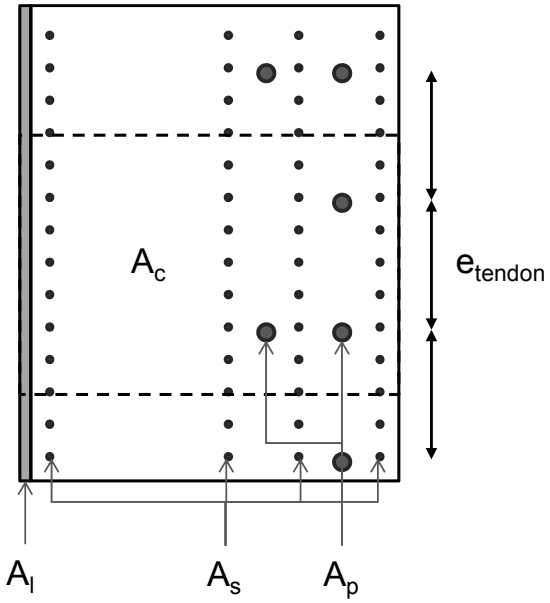

Figure 39. Containment building wall dimensions. A_p is the cross-sectional area of a horizontal tendon, $A_s$is the cross-sectional area of reinforcement steel, A_l is the cross-sectional area of the liner, $A_c$is the cross-sectional area of the share of concrete that each group of tendons compresses and e_{tendon} is the vertical distance between tendons.

Despite the tendons being grouped closer together vertically near the opening, as seen in fig. 36, the concrete area relative to the tendons stays approximately equal because the thickness of the wall is proportionally increased with the increase of tendon density in the vertical direction. Thus, the concrete cross-section is considered uniform along the tendon.

7.1.1 Instantaneous losses

According to EN 1992-1-1 section 5.10.5.2, friction losses along the length of the tendon are calculated as follows:

$$\Delta P_{\mu}(x) = P_{max}\left(1 - e^{-\mu(\theta + Kx)}\right), \tag{36}$$

where P_{max} is the tensioning force at the active end, μ is the friction coefficient, x is the distance from the end, θ is the cumulative change of angle of direction at point x and K is the unintended angular deviation per unit length (wobble).

The effect of anchor slip is calculated by determining the distance it takes friction to counteract the change in tendon length. That point has the highest value of the tensioning force of the tendon as shown in fig. 40. The other parameters used to calculate the stress state of the tendon are the ones used in the verification calculation. Their values are in table 7.

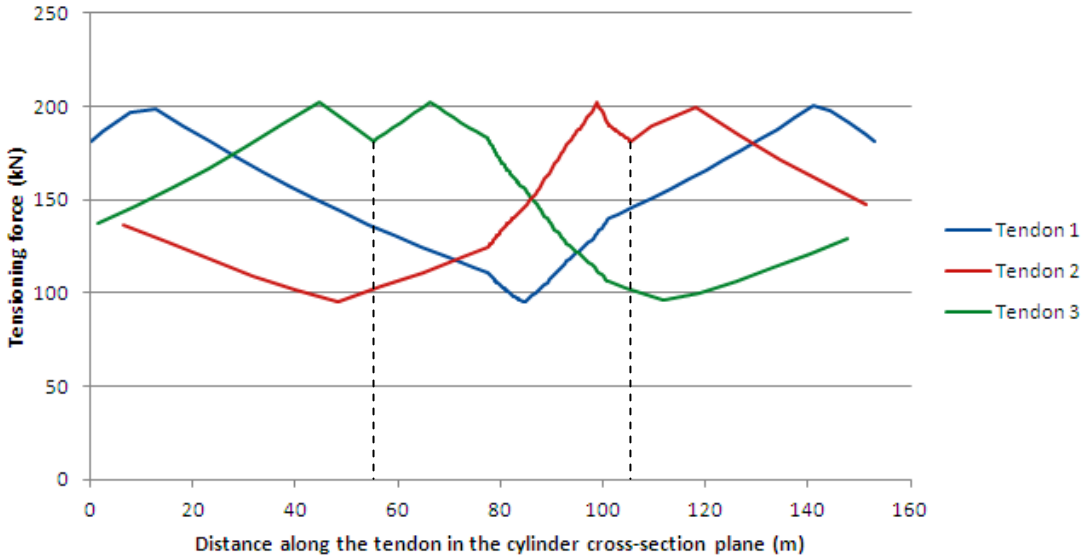

Figure 40. The tensioning force per strand in the tendons along the circumference of the cylinder. The tendons have starting points at buttresses located at 0 m, 55 m and 105 m. The 23.5 m area of effect caused by the equipment hatch is centred at 89.65 m.

The average tension force along the three tendons is used to calculate the average compression state of the concrete, steel reinforcement and the steel liner on the inner surface of the cylinder. The average tension of the otherwise identical tendons depends on the relative position of the deviation to the anchors. The average tension in a tendon is highest, when the deviation is exactly in the centre of the tendon.

The elastic shortening of the concrete is calculated from average compression of the cylinder with the following expression:

$$\Delta P_{ES} = A_p E_p \sum \left[\frac{j \cdot \Delta\sigma_c(t)}{E_{cm}(t)} \right], \tag{37}$$

where A_p is the cross-sectional area of the tendon, E_p is the modulus of elasticity of the tendon, $\Delta\sigma_c(t)$ is the change in compression in the concrete in the moment after tensioning, $E_{cm}(t)$ is the elastic modulus of concrete at the time of tensioning and j is a coefficient equal to

$$j = \frac{n_t - 1}{2n_t}, \tag{38}$$

where n_t is the number of tendons successively prestressed. It approaches 0.5 as n_t grows. Considering the tendons as groups of three would yield a value of 0.333, which should be considered as the minimum realistic value.

To calculate the cumulative change of angle of direction of the tendon, the path of the tendon is discretised using simple trigonometric functions to define the coordinates of the cylinder as in fig. 37 and parabolic equations to define the vertical deviation as in fig. 38. Successive points are treated as points defining a vector as shown in fig. 41.

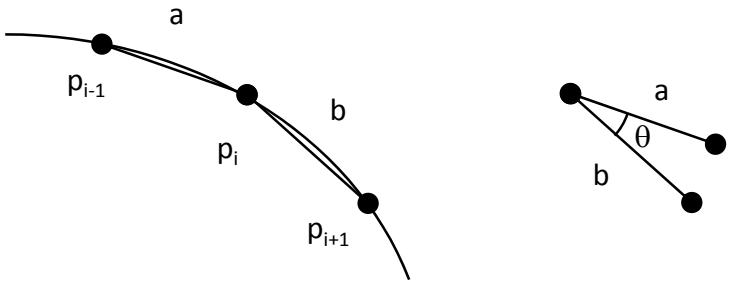

Figure 41. Discretation of the path of a tendon and the way the vectors are used to calculate the change of angle.

The angle between successive vectors' can be calculated with the following equation: (MAOL, 2013 p. 36)

$$\theta = \cos^{-1}\left(\frac{\bar{a} \cdot \bar{b}}{|a| \cdot |b|} \right), \tag{39}$$

where a and b are the vectors defined in the way previously described.

By forcing points infinitesimally close to parts of the tendon where the change in turning direction happens, i.e. half way from the maximum deviation to the base level, the discretation does not lose accuracy by "taking a shortcut". Figure 42

shows an example of the effect of the deviation on the cumulative change in angle of the tendon.

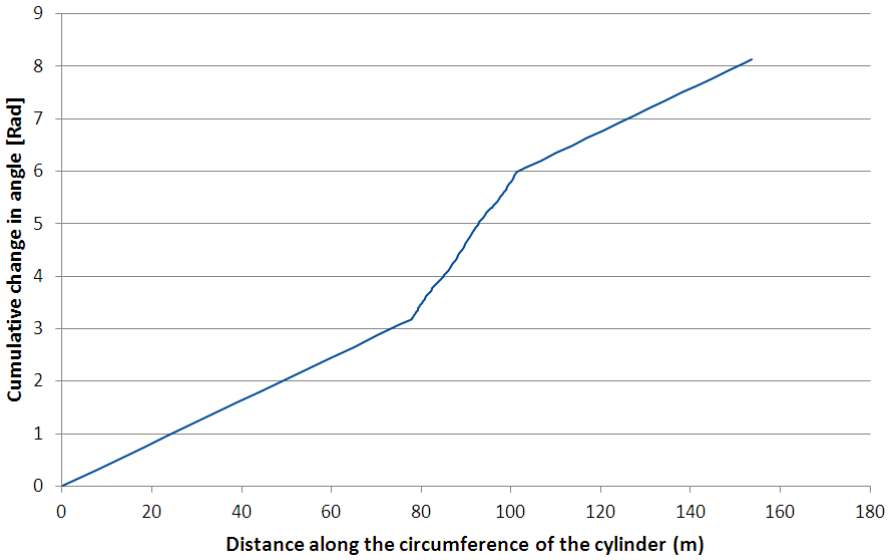

Figure 42. The effect of a 4.26 m vertical deviation on the cumulative change in angle of the tendon along the circumference of the cylinder.

Poisson's effect causes the wall to expand because of the vertical tensioning. The value of the average compression in the wall is taken to be the same as in the reference calculations.

7.1.2 Long-term effects

The four long-term effects affecting concrete are calculated according to EN-1992-2 appendix B. Autogenous shrinkage is an isotropic curing-related phenomenon affecting concrete. When the age of the concrete is over 28 days, autogenous shrinkage can be calculated using the following equation:

$$\varepsilon_{ca}(t) = (f_{ck} - 20)\left(2.8 - 1.1e^{-\frac{t}{96}}\right) \cdot 10^{-6}, \tag{40}$$

where f_{ck} is the strength of concrete in MPa and t is the age of the concrete in days.

Drying shrinkage is governed by changes in moisture content in the concrete, which depends on the relative humidity of the surrounding environment. It is calculated as follows:

$$\varepsilon_{cd}(t, t_0) = \frac{K(f_{ck})\left[72e^{-0{,}046 f_{ck}} + 75 - RH\right](t - t_0) \cdot 10^{-6}}{(t - t_0) + \beta_{cd} {h_0}^2}, \tag{41}$$

where $K(f_{ck})$ is the smaller of the following values 18 and $30 - 0.21f_{ck}$, where f_{ck} is in MPa, RH is the relative humidity, t is the age of the concrete, t_0 is the age of the concrete at tensioning, β_{cd} is 0.007 for silica-fume concrete and 0.021 for non silica-fume concrete and h_0 is twice the height of the concrete area per group of tendons.

Basic creep is anisotropic and influenced by the strength of the concrete and the strain state caused by loading, which, in the horizontal direction, is caused mainly by the prestressing. Drying creep is proportional to the initial strain state of the concrete and the drying shrinkage. The combined creep effects are calculated as follows:

$$\varepsilon_{cc}(t, t_0) = \frac{\sigma(t_0)}{E_c}[\varphi_b(t, t_0) + \varphi_d(t, t_0)], \tag{42}$$

where $\frac{\sigma(t_0)}{E_c}$ is the strain at the time of loading and $\varphi_b(t, t_0)$ is the basic creep factor and $\varphi_d(t, t_0)$ is the drying creep factor.

The basic creep factor is evaluated as follows:

$$\varphi_b(t, t_0) = \varphi_{b0}\frac{\sqrt{t - t_0}}{\sqrt{t - t_0} + \beta_{bc}}, \tag{43}$$

where

$$\varphi_{b0} = \begin{cases} \dfrac{3.6}{f_{cm}(t_0)^{0.37}} & \text{for silica} - \text{fume concrete} \\ 1.4 & \text{for non silica} - \text{fume concrete} \end{cases} \tag{44}$$

and

$$\beta_{bc} = \begin{cases} 0.37e^{2.8\frac{f_{cm}(t_0)}{f_{ck}}} & \text{for silica} - \text{fume concrete} \\ 0.4e^{3.1\frac{f_{cm}(t_0)}{f_{ck}}} & \text{for non silica} - \text{fume concrete} \end{cases} \tag{45}$$

In the above equations $f_{cm}(t_0)$ is the mean value of concrete cylinder strength at the time of loading. The drying creep factor $\varphi_d(t, t_0)$ is defined as

$$\varphi_d(t, t_\sigma) = \varphi_{d0}[\varepsilon_{cd}(t, t_0) - \varepsilon_{cd}(t_0, t_d)], \tag{46}$$

where t_d is the age at which drying begins and

$$\varphi_{d0} = \begin{cases} 1000 & \text{for silica} - \text{fume concrete} \\ 3200 & \text{for non silica} - \text{fume concrete} \end{cases} \quad (47)$$

Relaxation of the tendon under long-term tension can be estimated with the following equation:

$$\frac{\Delta\sigma_{pr}}{\sigma_{pr,i}} = 0.66 \cdot \rho_{1000} e^{9.1\mu} \cdot \left(\frac{t - t_\sigma}{1000}\right)^{0.75(1-\mu)} \cdot 10^{-5}, \quad (48)$$

where $\sigma_{pr,i}$ is the initial prestress in the tendon, ρ_{1000} is the relaxation at 20 °C in % after a 1000 hours specified by the manufacturer, $t - t_\sigma$ is the time after tensioning in hours and

$$\mu = \frac{\sigma_{pr,i}}{f_{pk}}, \quad (49)$$

where f_{pk} is the characteristic value of tensile strength in the prestressing steel.

7.2 Verification

The model is verified against calculations made by consultants for the OL3 project. (Bonneau, 2006) Their calculation is of a worst-case scenario with most of the parameters on the safe side. The model used was a large FEM model using material properties and shrinkage values specified in the Eurocodes. Table 7 lists the parameters used in the calculations as closely as they could be deciphered from the report.

Table 7. Parameters used in the calculation to verify the model against previous calculations by consultants on the OL3 project.

Tendon geometry			
Radius of the tendon's path	r	24,35	m
Length of the tendon	L	153,02	m
Location of the apex of the deviation along the circumference	_C	76,51	m
Length of tendon's deviation from plane leading to the obstacle	_l	10,58	m
Height of tendon's deviation	h_{dev}	0	m
Friction and wobble coefficients			
Friction coefficient	μ	0,18	-
Wobble	K	0,00162	-
Tendon properties			
Elastic modulus of the tendon	E_p	1,9E+11	Pa
Total cross-sectional area of the tendon	A_{ptot}	0,0081	m2
Number of strands in tendon	$n_{strands}$	54	-
Anchorage slip	Δ_A	0,008	m
Steel ultimate strength	f_{pk}	1,86E+09	Pa
Prestress initial	f_{p0}	1,49E+09	Pa
Relaxation loss after 1000h at 20C	ρ_{1000}	2,5	%
Tendon vertical distance	h_{tendon}	0,62	m
Concrete Properties			
Strength	f_{ck}	50	MPa
Type	s	0,25	-
Crossectional area per tendon	A_c	0,529	m2
Silica-fume	Silica	1	[1,0]
Modulus of elasticity	E_c	3,7E+10	Pa
Humidity	RH	20	%
Poisson's ratio	ν_c	0,2	-
Reinforcement and liner properties			
Reinforcement	E_s	2,1E+11	Pa
dReinforcement	d_s	32	mm
Distance between reinforcement bars	k	200	mm
Liner thickness	t_l	7	mm
Vertical loads (z-direction)			
Vertical location of tendon group (affects dead weight)	h_{tendon}	7,73	m
Deadweight+initial vertical tensioning	σ_{czG}	1,36	MPa
Dead weight and vertical prestressing	σ_{cztot}	9,23	MPa
Prestressing	σ_{czp}	7,87	MPa
Ratio of vertical tendons tensioned after the horizontal one		1	-
Time related factors			
Age when tensioned		365	d
EOL age		65	a

The results are very close to previously calculated values as is seen in table 8. Some of the error seems to be caused by a discrepancy in the amount of steel reinforcement. The amount of reinforcement was not stated in the preliminary calculations, but trial and error has revealed it to be slightly higher than the actual amount in final plans.

Table 8. Comparison of the calculated values to the reference calculation.

Name of value	Reference value	Calculated value	Ratio
Net initial tension in the tendons	955 MPa	982 MPa	1.028
Elastic loss	30.1 MPa	30.9 MPa	1.027
Initial stress state of the concrete	13.55 MPa	13.42 MPa	0.990
Loss of tension due to relaxation	16 MPa	17.8 MPa	1.113
Long-term losses due to creep and shrinkage	147 MPa	155.9 MPa	1.061

7.3 Analysis

With the calculation model verified, the parameters can be given distributions based on measured values from sample tests of the construction materials. A sample size of 6000 iterations was chosen to keep the resulting scatter plots sparse enough for visual estimation of the density of the result cloud. The computation time needed for this amount of iterations is around two minutes using a 2007-era laptop.

7.3.1 Parameters' distributions

The specifications of the prestressing system state that the coefficient of friction can vary 25% and that the initial tension of a single strand can be 5 % under or 8 % over the design tension. The whole tendon must be within 3 % of the design value. Anchor slip is specified as 4 to 8 mm. (Lehtimäki, 2010 p. 15)

The actual relaxation parameter of the tendon, ρ_{1000}, has been measured for tendons similar to the ones used in the OL3 project. The report by Bayart et al. (2010) reveals multiple measurements of the relaxation, which allows for rudimentary evaluation of the distribution of the values.

Concrete strength is continuously monitored at the OL3 construction site providing reliable data for creating a distribution for the concrete strength. Laboratory tests

are available for the modulus of elasticity (MOE) of the concrete in different relative humidity conditions.

Table 9 lists all the parameters that are given distributions. Any parameters not mentioned in it have the same values as in table 7. The result variables, which are made available for analysis, are listed in table 10.

Table 9. A list of the parameters used in the simulation. N signifies a normal distribution with parameters controlling the mean value and the variance. K signifies a triangular distribution with parameters defining the minimum value, mode and the maximum value. T signifies a uniform distribution, with parameters for minimum and maximum values.

Parameter		Distribution				
Name	Cell address	Symbol	Param. 1	Param. 2	Param. 3	Param. 4
Tendon's MOE E_p (Pa)	=Tendons!I3	N	1,9E+11	9,5E+09		
Friction coefficient μ (-)	=Tendons!D10	N	0,18	0,045		
Wobble factor k (-)	=Tendons!D11	N	0,0016	0,0004		
Tension at active jack f_{p0} (Pa)	=Tendons!I8	K	1,41E+09	1,49E+09	1,61E+09	
Relaxation ρ_{1000} (%)	=Tendons!I9	N	2	0,4		
Anchor slip (m)	=Tendons!I6	K	0,004	0,006	0,008	
Concrete strength f_{ck} (MPa)	=Tendons!N3	N	83	5		
Age when tensioned (d)	=Tendons!I15	N	365	50		
Vertical tension (MPa)	=Tendons!D17	N	7,87	1		
Relative humidity (%)	=Tendons!N8	K	35	50	65	
Height of deviation (m)	=Tendons!D7	T	0	6		

Table 10. Result variables whose values are saved for each iteration.

Results to be saved	
Name	Cell address
Initial prestress (MPa)	=Tendons!AC3
final prestress (MPa)	=Tendons!AC6
Elastic shortening (MPa)	=Tendons!AD10
Tendon relaxation (MPa)	=Tendons!AC11
Autogenous shrinkage (MPa)	=Tendons!AD12
Drying shrinkage (MPa)	=Tendons!AD13
Basic creep (MPa)	=Tendons!AD14
Drying creep (MPa)	=Tendons!AD15
Poisson's effect (MPa)	=Tendons!AD16
Pretensioning loss (%)	=Tendons!AC7
Loss of concrete tensioning (%)	=Tendons!AI7

7.3.2 Results

The results are divided into two parts, the first of which will investigate the parameters influencing the initial average stress state of the tendon after instantaneous losses. The second part investigates the parameters affecting the long-term losses.

The previously described input distributions lead to an output distribution for the initial average tension in the tendons shown in fig. 43. The mean value is 963 MPa and the standard deviation is 69.5 MPa.

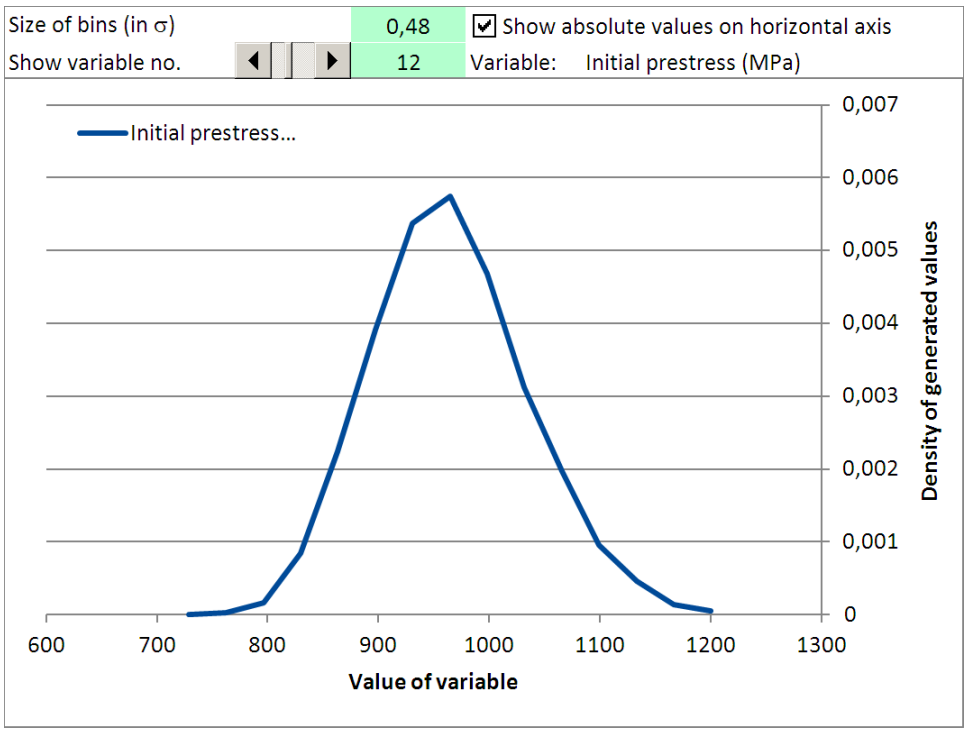

Figure 43. The density function of the average prestressing tension in the tendons after instantanous losses.

However, knowing which parameters cause most of the variance is more informative than the distribution. The results of the sensitivity analysis are presented in table 11. The significance values are calculated using equations (1) and (2). The friction coefficient is found to be the highest source of uncertainty in the model. This is because friction losses are the largest cause of losses in the initial stress state of the tendon and because the friction parameter has a high coefficient of variance (COV).

The tension at the jack directly correlates with the average tension in the tendon, but it has a much lower COV, which leads to it being the second largest source of uncertainty in the calculations. The wobble factor has a similar, but smaller, effect to the friction coefficient, which makes it the third most significant variable affecting the initial stress state of the tendon. Using the significance metric, changes in the

vertical deviation of the tendon have a smaller effect than the uncertainties of the previously mentioned variables. Other minor sources of uncertainty are the modulus of elasticity of the tendon and anchor slip. Although anchor slip is a significant phenomenon, the difference between the effects of a 4.8 mm and a 7.2 mm (the first and ninth deciles) slip on the average tension of the tendon is very small.

Five of the eleven distributed input parameters should not affect the initial stress state of the tendon, because they are used in the calculations that depend on the initial stress state. Their calculated significance values can therefore be interpreted as indicative of the error margins of the simulation. As the number of iterations increases, the significance values of the variables not affecting the stress state should converge to zero.

Table 11. Significance of the different input parameters, as defined in table 35, to the output parameter representing initial average tension in the tendon after instantaneous losses. The variables not affecting the initial tension are underlined.

Parameter	**Significance**	**Parameter**	**Significance**
Tendon's MOE	0.042	Concrete strength	0.003
Friction coefficient	1.000	Age when tensioned	0.009
Wobble	0.183	Vertical tensioning	0.032
Tension at jack	0.436	Relative humidity	0.025
Relaxation	0.002	Vertical deviation	0.102
Anchor slip	0.035		

The three most significant parameters' (friction coefficient, initial tension at the jack and wobble factor) scatter plots against the value of initial average tension in the tendon are shown in figs. 44 through 46. All three results show a clear slope in the trendline. For reference, a scatter plot of a non-significant parameter is visible in fig. 1 in appendix 3.

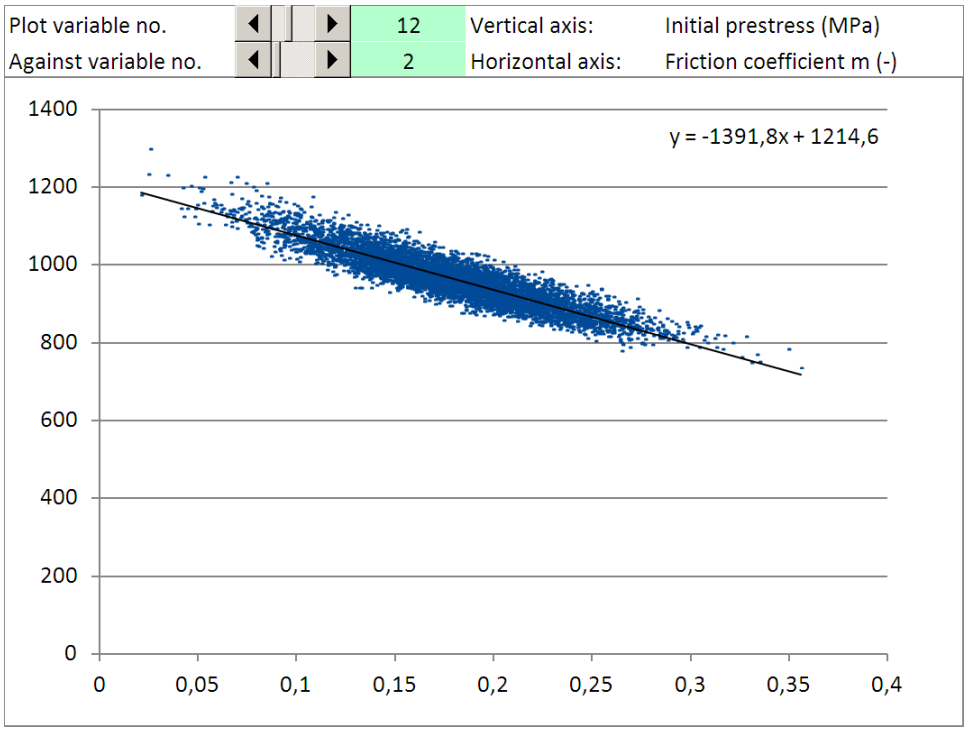

Figure 44. The friction coefficient is the dominant variable affecting the initial average tension in the tendons.

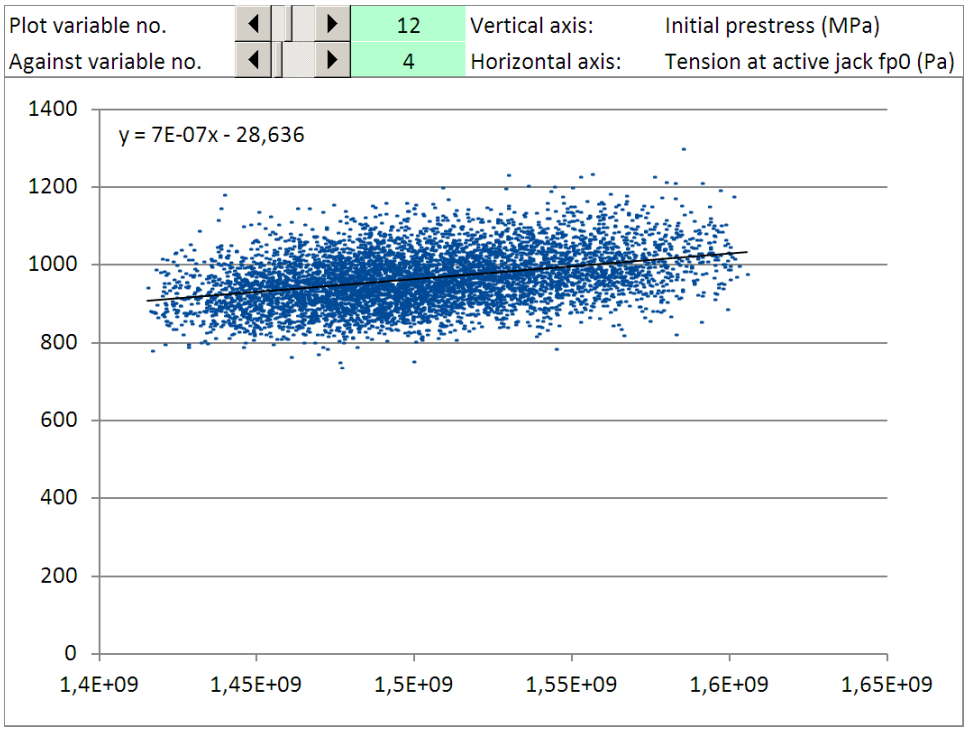

Figure 45. The tension at the active jack is a significant variable affecting the initial average tension in the tendons.

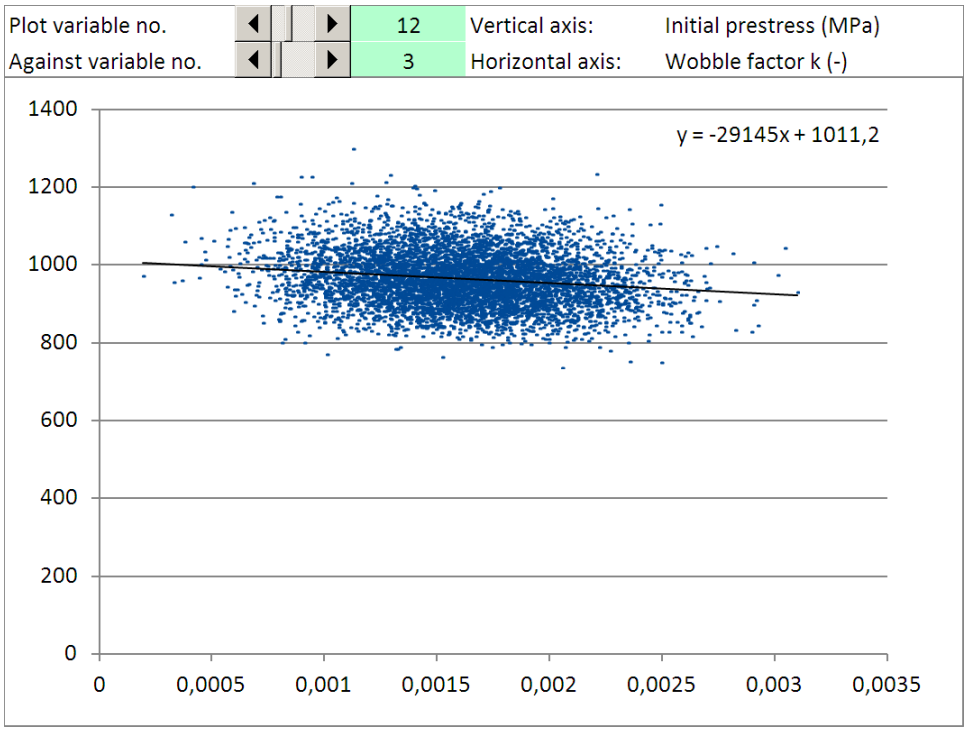

Figure 46. Like the friction coefficient, the wobble factor is a significant variable affecting the initial average tension in the tendons.

The second result variable to be analysed is the percentage of long-term losses of initial stress state of the tendon including instantaneous losses after tensioning. The distribution of the result variable in question is pictured in fig. 47.

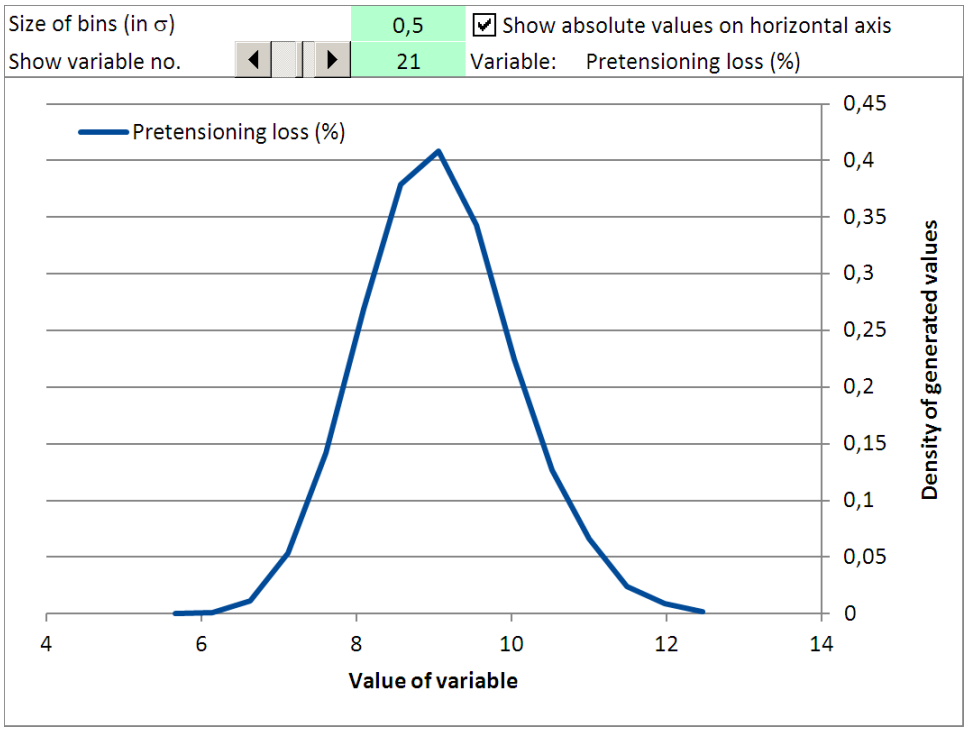

Figure 47. The distribution of the percentage of long-term losses of the initial tension in the tendons.

Again, the significance of each of the input parameters is calculated from the result data and is made available in table 12. The relative humidity of the environment the concrete is in is the most significant factor affecting the long-term loss of tension in the tendons, which is explained by the strong effect it has on the drying creep phenomenon. There are three other significant variables affecting the result variables, which are, in order of significance, concrete strength, the tendons modulus of elasticity and the 1000-hour relaxation parameter of the steel of tendon. The high significance of the MOE of the tendon could be lessened by giving its distribution a lower COV. This would be justified, because the material parameters of steel are well known and predictable. Hess et al. (2002, p. 43) have found that the COV of different experimental values of modulus of elasticity for structural steel averages 0.0179, which is well below 0.05, the value used for the generation of input variables. However, this may be different for the ultra-high-strength steel used in tendons.

Table 12. Significance of the different input parameters' effects on the output parameter, which represents the long-term loss of tension in the tendon as a percentage of the initial loss.

Parameter	Significance	Parameter	Significance
Tendon's MOE	0.483	Concrete strength	0.529
Friction coefficient	0.062	Age when tensioned	0.037
Wobble	0.005	Vertical tension	0.084
Initial tension	0.033	Relative humidity	1.000
Relaxation	0.346	Vertical deviation	0.001
Anchor slip	0.022		

Another interesting finding was that vertical tensioning done after the horizontal tendons have been tensioned can increase the average initial tension in a horizontal tendon through Poisson's effect by up to 1%. It has a small effect, but it is quantifiable with little effort. Its distribution, as seen in fig. 48, exactly mirrors the input distribution of the vertical tensioning variable, since the geometric properties of the structure are not varied.

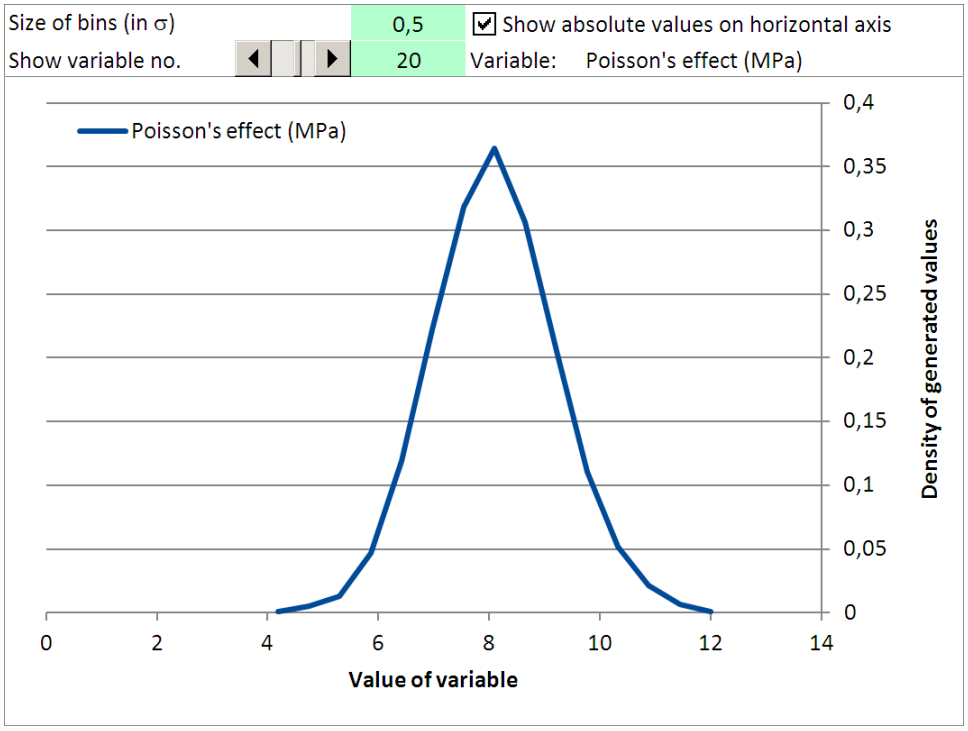

Figure 48. The impact of Poisson's effect on the average initial tension of the tendon.

In conclusion of this case study, the effect of the deviation of a tendon caused by an opening in the wall structure on the average tension in the tendons is very small. Especially when compared to the uncertainty in the values of the friction coefficient and, to a smaller degree, the uncertainties in the initial tension at the jacks used to tension the tendons. Long-term losses are most affected by the relative humidity of the environment and the strength of the concrete, which strongly affect creep and shrinkage of the concrete in the wall structure.

As a by-product of calculating the stress states of a tendon, the stress states of the concrete and the liner are also available. Interesting analyses, e.g. on the stress state of the liner after years of concrete shrinkage and creep, could be performed on both with little additional effort.

8 Conclusion

An easy-to-use Monte Carlo implementation was created that gives consistent and predictable results. Using a well-known spreadsheet program as the environment for the method shortens the learning curve of creating models and adopting the user interface. It is also possible to tap into the existing pool of created spreadsheet calculations and to perform analyses on them.

Two very different case studies were done. The first can be considered reminiscent of a decision-in-principle phase study, which explored the capabilities of a new type of structure. The second case is more on the lines of a construction license phase analysis.

The first case study ended up bordering too high a complexity level, with calculation times in excess of 60 seconds in certain cases. In addition, creating and especially verifying the many sub models was time-consuming. However, a model was created that could accurately model different kinds of failure mechanisms and many non-linear phenomena including cracking of the concrete and the yielding and sliding of studs and the steel plates.

The second case demonstrates the effectiveness of the tool in discovering the dominant sources of uncertainty when modelling a post-tensioning system. With the calculation model created and knowing what kinds of distributions to give input variables, setting up the Monte Carlo simulation is a matter of minutes. The input parameters are named and appointed a cell and given a distribution. The result variables only need to be named and appointed a cell. A few minutes of simulation later, concise significance values of the input variables' relationships to uncertainty in the result variables can be browsed through on the results page.

These analyses make it possible to find the significant factors affecting the results of a calculation model and the significant sources of uncertainty in-house. This information can be used to guide the contracting of TSOs for more detailed analyses. The licensee can also be requested to conduct experimental tests to back up design choices. Time spent on inspection work can be better allocated to avoid the identified insignificant phenomena.

Finding experimental data for the input parameters proved to be easy in these cases. Experiments and calculations were also readily available for benchmarking the created models. In future cases, the possible lack of experimental data could be addressed early on in the design and inspection process by requesting the necessary experiments.

Using the method enables taking a more active role in the inspection process. On the other hand, it requires bringing more modelling and structural analysis work in-house.

8.1 Steps needed for successful implementation of the review method

Before using the tool and method in practise, a cost-benefit study should be made to estimate the actual value of the tool. Data should be collected on how much time is spent on inspecting a certain type of structure and compared to the time spent creating a model and analysing it. Unfortunately, STUK does not have existing detailed statistics on the time spent during inspections. Had the data been available, its analysis would have been included in this thesis. The time spent creating and analysing the two types of structures in the case studies gives an estimate of how long creating new models can take.

The next verification stage of the methodology itself is done from a risk assessment point of view, in collaboration with specialists the risk assessment department, with their experience of and insight into uncertainty modelling and risk control. More rigorous statistical analysis tools might be easily available. The risk department will also be consulted on choice of subsequent cases.

8.2 Recommendations for future modules and cases

An efficient, linear FEM module could be made available with relatively little effort. The current implementation including non-linear capabilities is too complex and slow to calculate significant sample sizes in a timely manner. By removing the code that controls the iteration that achieves the non-linearity and by having all the calculation done on one spreadsheet, unnecessary recalculations would be reduced by orders of magnitude.

The next case under consideration is a seismic vibration resistance study of groups of components using a FEM methodology for dynamic modelling of a system with a limited number of degrees of freedom. The components have been tested against vibration individually, but their interaction with each other could cause lower failure criteria to appear. The group of components in question would be a pump unit and its base, which is comprised of a foundation, a motor, a pump and pipes. The scope of the case is to analyse six different pump units and use the results to commission a study from a TSO using complex FEM models.

The goal of the study is to reduce the amount of commissioned modelling work and improve the quality or relevance of the work order. Any reductions in the commissioned workload would quickly make the study pay for itself. The case is already at the data collecting stage, where it is ensured that enough input data is available for the modelling. The impetus for this analysis is derived from the new YVL-guides, which came into effect on 1.12.2013. The new YVL-guides B.7 states that, for the first time, “aggregates comprising electrical and I&C equipment, mechanical components, piping and equipment foundations shall be evaluated in such a way that, in addition to the verification of the seismic qualification of indi-

vidual components, interactions between these components are also taken into account.”

9 References

Agarwal, D.C. (2012) DOE Graded Approach. IAEA January 23-27, 2012 Meeting. IAEA headquarters, Vienna, Austria. [Online] Available from: http://www.iaea.org/NuclearPower/Downloadable/Meetings/2012/2012-01-23-01-27-TM-NPE/USA-GradedApproach.pdf [Accessed: 15th April 2014]

Agarwal, R.B. (2014) *Chapter 4 – Beam Element*, ME 273-01, [Lecture handouts] Finite element methods in engineering, San Jose State University, Department of Mechanical and Aerospace Engineering, Spring 2014

Ang, A & Tang, W. (2007) *Probability Concepts in Engineering Planning and Design Vol. I: Basic Principles.* 2nd Edition. John Wiley and Sons inc. ISBN-13 987-0-471-72064-5

Bayart, C. & Henriet, G. (Université catholique de Louvain Laboratoire du Génie Civil) (2010) *RE: Extrapolation from short term test to 1000 hours relaxation.* [Letter] Receiver: Lucas, J-R. (Freyssinet International & CIE) 9th June 2010.

Bonneau, J. (2006) *Detail Design of Prestressed Containment Model Description and General Design Criteria.*

DIBT (Deutches Institut für Bautechnik) (2003) *European Technical Approval for NELSON-headed studs* ETA 03/0041. [Online] Available from: www.nelson-europe.co.uk/approval.pdf [Accessed: 12th May 2014]

Hess, P.E., Bruchman, D., Assakkaf, I.A. & Ayyub, B.M (2002) *Uncertainties in Material Strength, Geometric, and Load Variables.* Naval Engineers Journal, ASNE. [Online] Available from: http://assakkaf.com/Papers/Journals/Uncertainties_in_Material_Strength_Geometric_and_Load_Variables.pdf [Accessed: 8th May 2014]

IAEA. (2014) *The Power Reactor Information System.* [Online] Available from: www.iaea.org/pris [Accessed: 8th April 2014]

JEA (Japan Electrical Association). (2010) *Technical Code for Aseismic Design of Steel Plate Reinforced Concrete Structures JEAC 4618-2008:2010 Public Review Edition*.

Lehtimäki, J. (2010) *Specification for the prestressing system of OL3 EPR*

Leskelä, M. (1986) *Calculation Models for Concrete-Steel composite Beams, Considering Partial Interaction. A* Thesis Submitted in partial fulfilment of the Requirements of Oulu University for the Degree of Doctor of Science. Oulu: Oulu University.

MAOL. (2013) *Maol taulukot.* Keuruu: Otavan kirjapaino Oy. ISBN 978-951-1-26270-1

Mazaheri, A. (2013) *Monte-Carlo Simulation*. KUL-24.4200 Introduction to Risk Analysis of Structures P. [Lecture Notes] Aalto University. School of Engineering. Department of Applied Mechanics. 23rd February 2014

McCullough, B. D. (2008) Microsoft Excel's 'Not The Wichman-Hill' random number generators. *Computational Statistics & Data Analysis.* [Online] (52/10). p. 4587-4593. Available from: http://dx.doi.org/10.1016/j.csda.2008.03.006 [Accessed: 6th February 2014]

McKinley, B. & Boswell, L.F. (2002) Behaviour of double skin composite construction. *Journal of Constructional Steel Research.* [Online] (58/10). p. 1347–1359. ISSN:0143-974X Available from: http://dx.doi.org/10.1016/S0143-974X(02)00015-9 [Accessed: 13th January 2014]

Mishra, G. (201?) *Circular Prestressing.* [Online] Available from: http://theconstructor.org/concrete/prestressed/circular-prestressing/1521/ [Accessed: 8th April 2014]

Schnütgen, B. (2011) *Final Test Report of Creep, Shrinkage and E-modulus of Concrete Mixes used for Inner Containment 30UJA.*

SFS. (2005) SFS-EN 1992-1-1:2004 *Eurocode 2: Design of concrete structures. Part 1-1: General rules and rules for buildings*. Helsinki: Finnish standards association.

SFS. (2006) SFS-EN 1992-2:2005 *Eurocode 2: Design of concrete structures. Concrete bridges. Design and detailing rules*. Helsinki: Finnish standards association.

STUK (2013a) YVL B.2 Available: http://www.finlex.fi/data/normit/41401-YVL_B.2.pdf [Accessed: 8th April 2014] ISBN 978-952-478-857-1

STUK (2013b) YVL E.6 Available: http://www.finlex.fi/data/normit/41446-YVL_E.6.pdf [Accessed: 8th April 2014] ISBN 978-952-478-950-9

Varpasuo, P. (2002) *The Design and Analysis of Tianwan NPP Reactor Containment According to Design Basis and Beyond Design Basis Condition* [Online] Available from: http://www.kolumbus.fi/pentti.varpasuo/ned02.htm [Accessed: 28th April 2014]

Appendix 1: The pseudo code for the modified bisection algorithm for calculating the secant modulus of the steel plates

```
roundnmbr=0                 //The variable containing the number of iterations so far
consecpos=0       //Number of consecutive rounds, after which the secant modulus has been increased
consecminus=0     //Number of consecutive rounds, after which the secant modulus has been decreased
maxiter=40                  //The maximum number of iterations

max=E.s                     //The initial bounds of the bisection algorithm E.s=MOE of the steel plate
min=0
RunFEM                      //The stresses and strains are calculated after the first run

for i=0 to maxiter                          //Non-linear effects are achieved with this iteration
      if tolerance < 0,1%   //If the strain state matches the stress state, end iteration
            end for
      roundnmbr++

      Effects of cracking   //Elements adjusted according to the procedure in chapter 6.3.4
      Effects of Studs      //Elements adjusted according to the procedure in chapter 6.3.2

      if (sec.M.ss<E.s)     //sec.M.ss is calculated from the strain state and the material model
            sec.M= (max-min)/2  //sec.M is the value given to the steel plates for the next iteration
      else
            sec.M= E.s
              RunFEM

      if sec.M.ss< sec.M
                                max = sec.M.ss
                                consecpos=0
            consecneg++     //increase the count of consecutive iterations where sec.M.ss< sec.M
              else
                                min = sec.M.ss
                                consecneg=0
            consecpos++     //increase the count of consecutive iterations where sec.M.ss < sec.M
```

//If sec.M.ss is larger than sec.M many times in a row or smaller than sec.M many times in a row, it is possible that the correct value has moved outside the bounds min and max. This can happen because cracking changes the distribution of stresses in the structure. The figure below shows this phenomenon happening in the green, yellow and dotted lines. The solution is to widen the search area after a number of consecutive smaller or larger sec.M.ss values. The amount the search area is widened decrease with amount of iterations, so that the algorithm does not end up jumping back and forth over the correct value as happens to the dotted line in the figure below.

```
      M=20/(roundnmbr+5)  //A factor that decreases according to the round number
      if consecpos>4      //After 5 consecutive increases  in sec.M the search area is widened
            max=max*(1+0,15*M)
            min=min*(1-0,05*M)
```

```
        consecpos = consecpos – 2       //The number of consecutive decreases is lowered, but not
                                        to zero so that the next widening of the search area in the
                                        same direction comes more quickly, if it is necessary.
        if consecneg>4          //After 5 consecutive decreases in sec.M the search area is widened
                max = max / (1-0,05*M)
                min = min / (1 + 0,15*M)
                consecneg = consecneg -2
next i                                                  //Back to the beginning of the for-loop
```

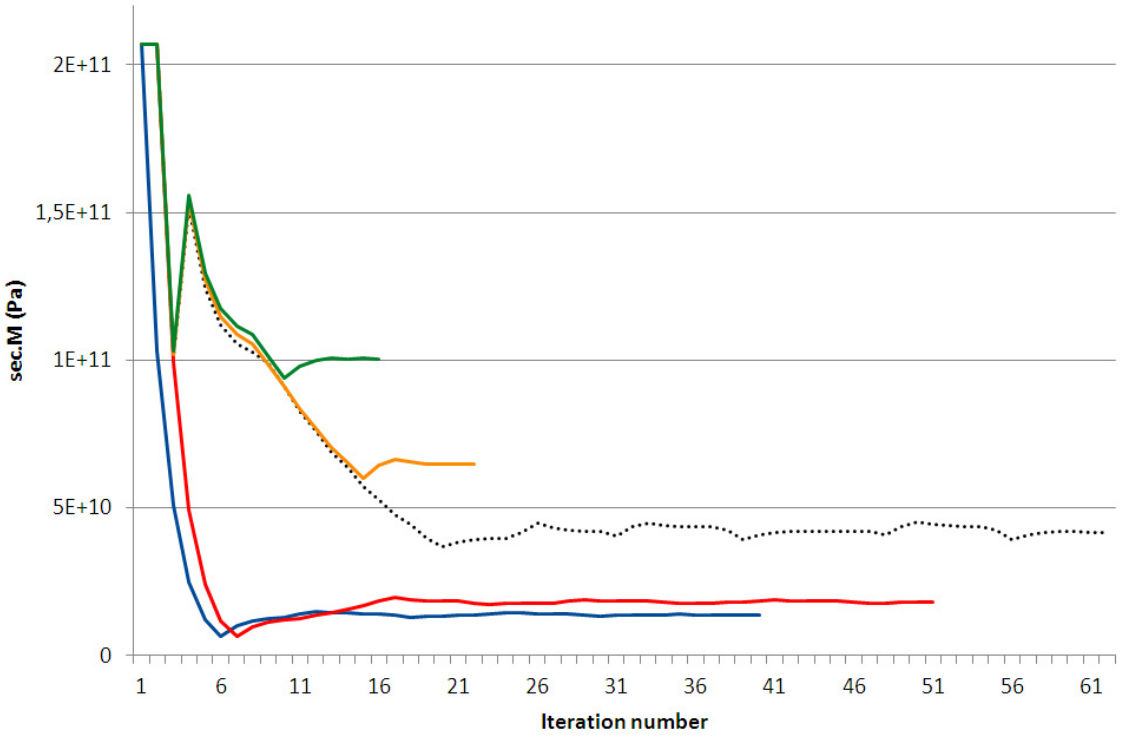

Figure 1. The modified bisection method in action. The vertical axis represents the secant modulus at each stage in the iteration. The horizontal axis represents the number of iterations. Each line represents the trial values of sec.M at each stage of the iteration.

The blue line settles to the lowest secant module value of the steel plates. This means the most yielding has happened and the force loading the structure was the largest of these simulations. It is just enough larger than the load on the red line to cause the steel to reach a yielding strain using the full cross-section of concrete, even before the effects of cracking reduce it. That is why the blue line starts to decrease earlier than the others.

The tolerance used was 0,1 %, which is unnecessarily tight considering the coarseness of the model in general.

Appendix 2: Visualisation of the elements and their deformations

The structure is drawn in its initial and deformed states using the chart feature in Excel. This is can be done by plotting the original an deformed end coordinates of the elements as a series on a scatter plot. This is linear interpolation.

To better visualise the rotational deformations of the elements end nodes, deflections along the elements are interpolated using a third order function. The deflection along the element in the element's local coordinates takes the form of

$$v(x) = Ax^3 + Bx^2 + Cx + D \tag{50}$$

where the variables A, B, C and D can be solved from the following border conditions with the values in local coordinates using the nomenclature in fig. 24:

$$\begin{cases} v(0) = v_1 \\ v(L) = v_2 \end{cases}, \quad \begin{cases} \dot{v}(0) = \varphi_1 \\ \dot{v}(L) = \varphi_2 \end{cases} \tag{51}$$

Solving the system of equations yields:

$$\begin{aligned} A &= \frac{2(v_1 - v_2) + L(\varphi_1 + \varphi_2)}{L^3} \\ B &= \frac{3(v_2 - v_1) - L(2\varphi_1 + \varphi_2)}{L^2} \\ C &= \varphi_1 \\ D &= v_1 \end{aligned} \tag{52}$$

The deformation curve per element is transformed into global coordinates. The change in the length of an element is accounted for by the following equation

$$L = L_0 + u_2 - u_1 \tag{53}$$

where L_0 is the original length of the element. The benefits of higher order interpolation are visible in the figure below.

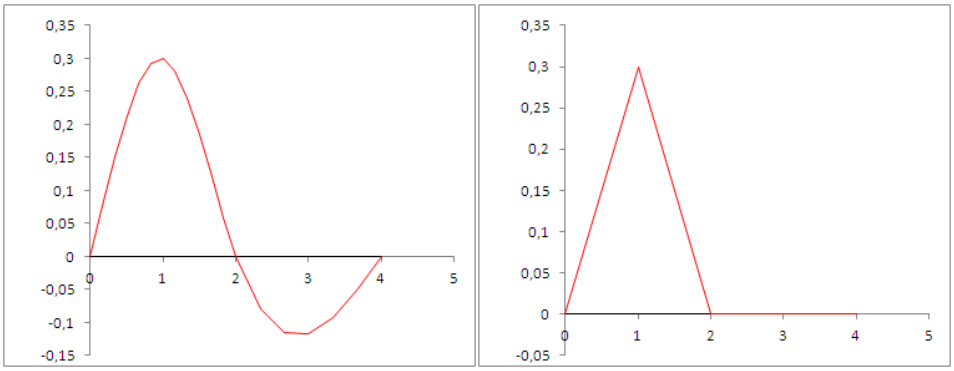

Figure 1. The red curves represent a deformed beam that was loaded by a vertical force at node (1,0). The beam is defined by three elements, with nodes at (0,0), (1,0), (2,0) and (4,0). All nodes except (1,0) have pinned supports. The left side shows the deformation using cubic interpolation and the right side using linear interpolation.

Appendix 3: Additional scatter plots for the tendon case

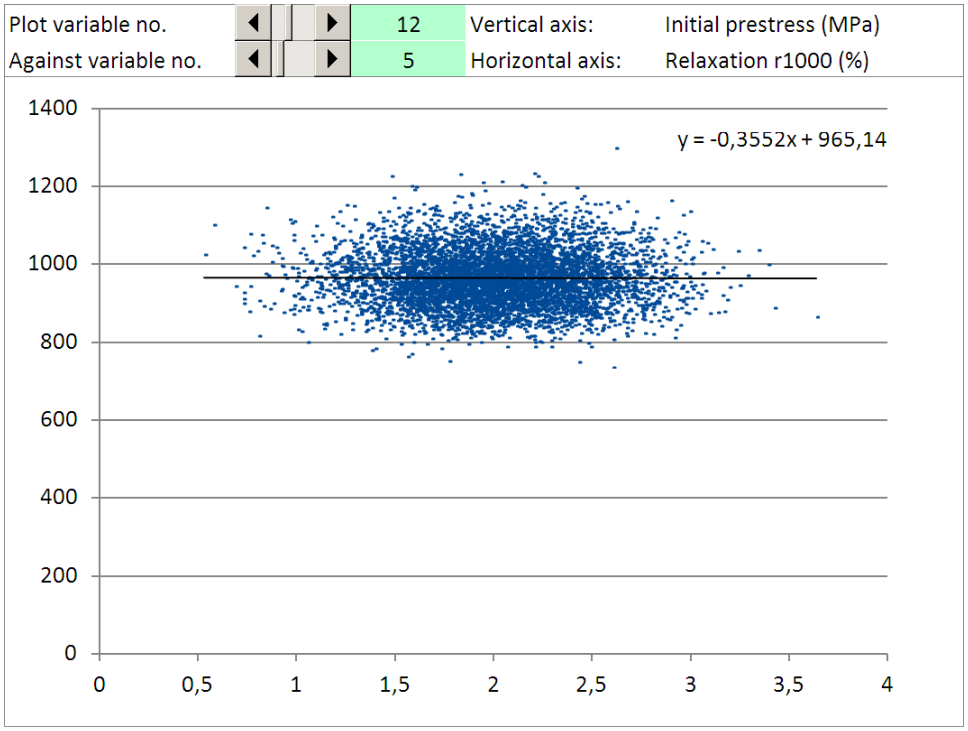

Figure 1. A scatter plot showing a non-significant relationship.

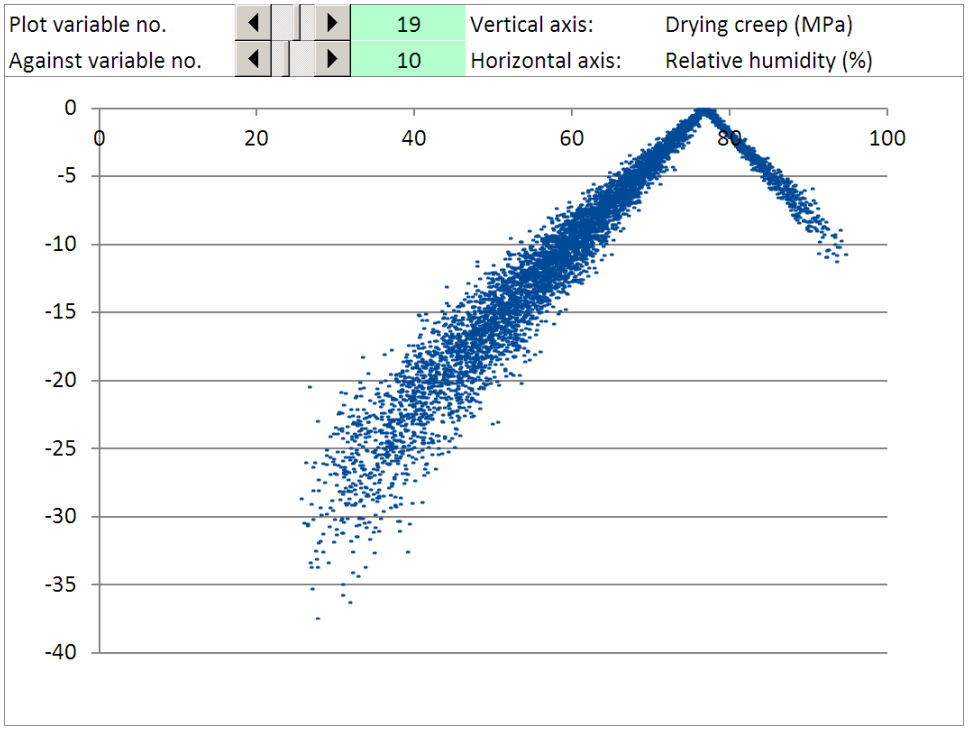

Figure 2. A scatter plot showing a relationship, whose significance evaluation requires special attention.